university of groningen / faculty of science and engineering / kapteyn astronomical institute

Master Research Project

Rijksuniversiteit Groningen

Kapteyn Astronomical Institute

Disentangling Chemodynamic Populations in the Sextans dSph:

Demonstrating the Combined Power of Astrometry, Photometry, and Spectroscopy

Thom P. van Essen

S3169308

Supervisor:

Eline Tolstoy

Second Examiner:

Else Starkenburg

Coordinator:

Inga Kamp

July 25, 2022

Abstract

While it is widely believed in ΛCDM cosmology that dwarf galaxies are the building blocks of massive galaxies like our own Milky Way, our understanding on their formation and evolution remains foggy. Moreover, dSph galaxies are the most ubiquitous type of galaxy in the present-day universe. All the more reason to investigate them in detail. In this thesis the Sextans dSph will be examined in detail through a combination of astrometry, photometry, and low- and high resolution spectroscopy. Its kinematics are examined in detail, revealing a velocity gradient consistent with rotation about the minor axis of the system. A previously reported ring-structure with a distinct velocity is found. The chemodynamic stellar populations in Sextans are analysed in detail, showing that the ring-structure is responsible for the bulk of the metal-rich stars in Sextans. Possible scenario's on the formation of the ring are discussed, but a clear possibility is not found.

Contents

Chapter 1

Introduction

In the current ΛCDM cosmological paradigm, galaxies form through cooling and condensation of baryons in dark-matter haloes that merge hierarchically to build more massive galaxies (White and Rees, 1978). From this point of view it is vital to build a firm understanding of how dwarf galaxies, believed to be the first building blocks of massive galaxies, are formed and evolve, both in isolation but also as neighbours of massive galaxies like the Milky Way or M31. Besides their importance in galaxy assembly scenarios, dwarf galaxies serve as some of the best astrophysical laboratories to study the nature of dark matter and the structure of dark-matter haloes due to their typically very high mass-to-light ratios (Battaglia and Nipoti, 2022).

1.1 The Importance of Dwarf Spheroidals

In the present-day universe, dwarf spheroidal (dSph) galaxies are the most common type of galaxy. They are the least massive, least luminous, and most dark-matter dominated systems found (Tolstoy et al., 2009; McConnachie, 2012, for a review on their properties). Locally found as satellites in the outer parts of the Milky Way and M31, dSphs are gas-deficient, early-type systems where a morphology-density (Dressler, 1980) relation suggests they have been subjected to environmental effects and tidal gravitational fields (e.g. Mayer et al., 2001; Sawala et al., 2012; Poulain et al., 2021).

Typically thought to have simple stellar populations (e.g. Grebel and Gallagher, 2004), dSphs have been considered to be the surviving building blocks of Milky Way or M31 (Rodriguez-Gomez et al., 2016, and references therein). Thus, the stellar populations of dSph are a useful probe of the star formation and chemical enrichment in low-mass galaxies and the impact of environmental effects. To date there have been numerous detailed spectroscopic studies of classical dSphs. These studies are based on resolved stellar populations and include low resolution spectroscopy of a large number of stars to deduce kinematic and chemical properties of the stellar populations (e.g. Tolstoy et al., 2004; Battaglia et al., 2006; Walker et al., 2007; Battaglia et al., 2008; Walker et al., 2009; Battaglia et al., 2011) and high resolution spectroscopy of smaller numbers of stars to study the chemical enrichment and the production sites of heavy elements (e.g. Reichert et al., 2020; Theler et al., 2020; Mashonkina et al., 2022). Deep photometric studies of dSphs and subsequent colour-magnitude diagram (CMD) analysis revealed a similar story: the stellar populations of dSphs are typically ancient and formed in bursty star formation episodes early on in the life of these systems (e.g. Lee et al., 2009; Bettinelli et al., 2018, 2019; Rusakov et al., 2021). Being able to study the stellar populations star-by-star through their line-of-sight velocities, metallicity (either from photometry, low resolution spectroscopy, or high resolution spectroscopy), and chemical abundances of a range of elements is fundamental to all of these studies.

Later detailed studies of the stellar populations in dSphs show that their stellar populations are not as simple as initially thought, often hosting a diffuse and metal-poor component with a centrally concentrated, metal-rich population (e.g. Tolstoy et al., 2004; Koch et al., 2006; Taibi et al., 2018;

Pace et al., 2020; Alfaro-Cuello et al., 2020). Observationally this manifests as a metallicity gradient within the galaxy. Battaglia et al. (2006) and Amorisco and Evans (2012) showed that the star-formation history (SFH) of dSphs can be even more complex by modelling the stellar population of Fornax as a superposition of three distinct chemodynamical subpopulations.

Substructures in dSphs have been an ongoing search over many years. Stellar clusters and kinematic substructures are the easiest types to distinguish either based on increased stellar densities or significantly different kinematic signatures which can be found using accurate (low resolution) spectroscopy. Thus far globular clusters have been found in Sagittarius (Law and Majewski, 2010), Fornax (Buonanno et al., 1998; Larsen et al., 2012), and Eridanus II (Zoutendijk et al., 2020; Simon et al., 2021). The coincidence of the most massive globular cluster with the position of the centre in Sagittarius has led to the belief that it might be the nucleus of the galaxy (Sarajedini and Layden, 1995). Other substructures in dSphs, typically manifesting as clumps of stars with low velocity dispersions, have been found in Carina (Lora et al., 2019), Sextans (Kleyna et al., 2004; Walker et al., 2006; Kim et al., 2019; Lora et al., 2019), and Ursa Minor (Kleyna et al., 1998). Pace et al. (2014) demonstrated the power of Bayesian object detection methods in disentangling kinematic substructures in dSphs by applying them to Ursa Minor, being able to distinguish two distinct structures: one with a very small velocity dispersion compared to the rest of the galaxy, and one with a significantly different velocity.

As one of the nine pre-SDSS (Sloan Digital Sky Survey) dSphs around the Milky Way, Sextans' discovery came in 1990 (Irwin et al., 1990), being only second to last to Sagittarius (Ibata et al., 1994). Due to its large spatial extent, low surface brightness, and position behind the Galactic disk, the Sextans dSph is hard to observe even though it is relatively close to the Milky Way (Irwin and Hatzidimitriou, 1995). Detailed studies of the CMD reveal a stellar population dominated by old, metal poor stars (Lee et al., 2009). Spectroscopic follow up using the Calcium triplet lines to determine metallicities shows indications of two kinematically distinct stellar populations (Battaglia et al., 2011) as was previously found in other systems. Recent deep photometric studies found no evidence of tidal disturbances or substructures in Sextans (Cicuéndez et al., 2018). However, it was found that the stellar population is more centrally concentrated than previously thought. The spectroscopy combined with deep photometry also showed the presence of a ring-like substructure with a distinct velocity compared to the main body of Sextans (Cicuéndez and Battaglia, 2018). This ring-structure has been interpreted as the remnant of a recent merger event.

The first high resolution spectroscopic studies had very limited sample sizes, usually only a few stars were observed (e.g. Mashonkina et al., 2017a,b; Lucchesi et al., 2020). With the advent of multiplexing in high resolution spectroscopy larger homogeneous sample sizes became available (Theler et al., 2020). These high resolution studies showed that systems with varying SFHs can have similar chemical signatures, especially in the alpha-elements Mg, Ca, and Ti (Theler et al., 2020) but with considerable differences in the scatter between systems (Reichert et al., 2020). Trends in the Iron-peak and neutron-capture elements give valuable insights into the production sites of these elements and the yields of different elements in supernovae events in a dwarf galaxy environment (also Theler et al., 2020).

Over the years cosmological simulations have become an important tool to study the formation and evolution of (dwarf) galaxies. Early simulations suffered from multiple issues mainly related to poor implementation of sub-grid physical processes like stellar feedback and supernovae, and the influence of the cosmological UV background (e.g. Dekel and Silk, 1986; Efstathiou, 1992; Kravtsov et al., 2004; Stinson et al., 2006). Coupled with a strong effect of the numerical resolution of a simulation, this led to simulations not being very reliable initially. Over the years they have become incredibly powerful tools to study the details of dwarf galaxies with Revaz and Jablonka (2018) showing that the observed diversity of Milky Way satellites arises naturally in a ΛCDM universe, a result already reported by Kauffmann et al. (1993).

If we wish to understand the formation of dwarf galaxies, in particular dwarf spheroidals, and the assembly of massive galaxies in a ΛCDM universe more thoroughly a detailed understanding of the present dwarf spheroidals is essential. This is where this thesis focusses on, in particular a

(chemo)dynamical analysis of the Sextans dSph. First the used data will be presented in Chapter 2 followed by the method used to select members of the Sextans dSph in the data catalogue in Chapter 3. Kinematic and chemical analyses are conducted separately in Chapters 4 and 5, respectively, before combining their powers for a chemodynamical analysis in Chapter 6.

1.2 What is a Dwarf Galaxy

In recent decades strong efforts were made to discover, count, characterise, and quantify the impact of these small galactic systems within the local universe (Tolstoy et al., 2009; Sawala et al., 2016; Simon, 2019). Especially with the advent of digital sky surveys like the Sloan Digital Sky Survey (SDSS York et al., 2000) this has led to a zoo of 'new' classes of small galactic systems ranging from the rather diffuse, passively evolving dwarf spheroidals (dSph) to actively star-forming blue compact dwarfs (BCD). Therefore it is fitting to present a brief overview of dwarf galaxy taxonomy. However, first a working definition to discern dwarf galaxies from globular clusters on the low-mass end and traditional galaxies on the high-mass end is needed.

Tammann (1994) gave a strong definition of a dwarf galaxy: any coherent group of stars less luminous than $M_B = -16.0$ and more spatially extended than a globular cluster is considered a dwarf galaxy. However, this brings to question the upper limit on the size of globular clusters and hence the lower limit of dwarf galaxy size. If this definition is combined with the definition of a galaxy: any gravitationally bound collection of stars whose dynamics can not be explained through a combination of baryons and Newton's laws of gravity (i.e. dark matter must be present Willman and Strader, 2012) a more robust definition of a dwarf galaxy can be established. As such the common definition of a dwarf galaxy is: any collection of gravitationally bound stars less luminous than $M_B = -16.0$ whose dynamics can not be explained in the absence of a considerable amount of dark matter is considered a dwarf galaxy. Naturally this would exclude GCs as they are traditionally believed to be devoid of dark matter (e.g. Bradford et al., 2011; Carlberg and Grillmair, 2021) even though their dark matter content has been placed under scrutiny (e.g. Ibata et al., 2013; Bianchini et al., 2019).

Dwarf galaxies come in many different shapes and sizes. The classic dichotomy between early and late-type galaxies can also be applied to dwarf galaxies (ETGs and LTGs, respectively). Early-types include dwarf ellipticals (dE), dwarf spheroidals (dSph), the ultra faint dwarfs (UFD) and ultra compact dwarfs (UCD). All galaxies that show little to no ongoing star formation. Late-types on the other hand have significant star formation and can experience bursts of star formation. Dwarf irregulars (dIrr) and blue compact dwarfs (BCD) make up the late-type dwarf galaxies. Figure 1.1 shows the central surface brightness-absolute magnitude plane and how the different types of galaxy follow relations on this plane.

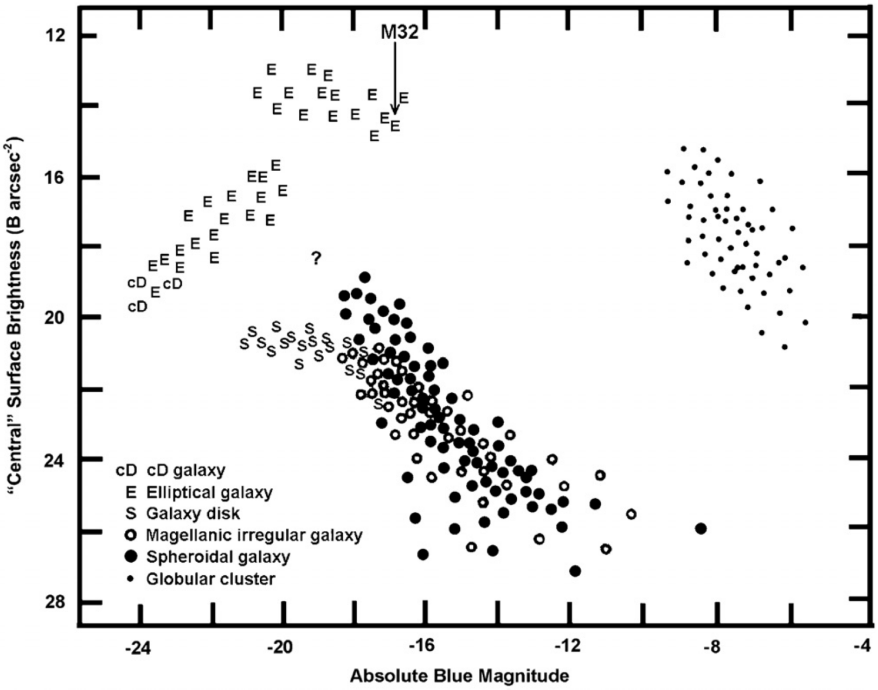

FIGURE 1.1: The correlation between absolute blue magnitude and central surface brightness for different classes of galaxies Illustrating the distinction between (dwarf) ellipticals and (dwarf) spheroidals. Figure from Kormendy et al., 2009.

Chapter 2

Data Description

In this chapter the data used in this thesis will be described. It consists of three parts to allow a detailed understanding of the chemodynamical properties of the Sextans dwarf spheroidal galaxy based on the properties of its Red Giant Branch (RGB) stars. The first part of the dataset consists of low resolution spectroscopic data from the GIRAFFE (Grating Instrument for Radiation Analysis with a Fibre Fed Echelle) spectrograph mounted on the European Very Large Telescope Fibre Large Array Multi Element Spectrograph (VLT/FLAMES), and a small additional dataset from the Michigan/Mike Fibre System (MMFS) fed by the Magellan/Clay telescope, hereafter the FLAMES and MMFS dataset, respectively. The second part of the data incorporates high resolution spectra from the GIRAFFE and UVES spectrographs, used to determine detailed chemical abundances. Finally, photometry and astrometry from the European GAIA mission is used, in particular the Early Data Release 3 (EDR3) released in December 2020 (Gaia Collaboration et al., 2021).

2.1 Low Resolution Spectroscopy

The goal of low resolution spectroscopy is to obtain reliable radial velocities and to determine Iron abundances using an indicator such as the calcium triplet (CaT) or the magnesium triplet (MgT) absorption lines.

The FLAMES observations were carried out at a variety of different times. Initially observations were made between 2003 and 2004, one field was re-observed in May 2008, with additional observations made in March 2019. The data from the first observations have been published by Battaglia et al. (2011). The second run consists of 25 additional pointings to increase the spatial coverage of the observations. The log of these pointings can be found in Table 2.1. The GIRAFFE spectrograph was used with grating LR8 which covers the wavelength range $8204-9400\,\text{Å}$ with a resolving power $R \sim 6,500$. The wavelength region contains the Calcium triplet (CaT) lines which are used to obtain radial velocities and determine metallicities. All of the spectra have been (re-)reduced in a consistent way to obtain a uniform dataset. The first step used the modern ESO data reduction pipeline (Freudling et al., 2013) which removes instrumental signatures and cosmic ray hits. After this, the spectra are processed further using code provided by Mike Irwin which takes care of sky-subtraction and extracts radial velocities and equivalent widths for the Calcium triplet lines.

The complete sample of FLAMES observations consists of 2222 individual spectra. Quality cuts were imposed on the signal-to-noise ratio, requiring it to be at least 7, and on the inferred radial velocity, for which the error should be no greater than $5\,\text{km s}^{-1}$, in order to avoid inaccurate measurements. After combining the results for targets that were observed multiple times, the final sample size is 1840 targets with a mean radial velocity error of $0.78\,\text{km s}^{-1}$. Metallicities were obtained from the CaT equivalent widths using the calibration developed by Starkenburg et al. (2010). This scaling relation was tested for metallicities down to $-4\,\text{dex}$ and yields typical uncertainties of $0.1\,\text{dex}$ or lower. The spatial distribution of this dataset is shown in the leftmost panel of Figure 2.1.

TABLE 2.1: Journal of VLT/FLAMES pointings of the 2019 run at R $\sim 6,500$. The columns give the name of the observed field, the coordinates of the pointing in Right Ascension and Declination, the UT date of the pointing and the exposure time of the pointing in seconds.

Fieldname	R.A. [J2000]	Decl. [J2000]	Date	Exposure time [sec]
Sextans-Pal3-extra	10:05:29.0	00:00:33.6	2019-03-12	3600
Sextans-c11	10:07:31.7	-00:03:01.1	2019-03-12	3600
Sextans-c12	10:08:45.0	-00:26:55.6	2019-03-13	3600
Sextans-c13	10:05:27.9	-01:23:51.8	2019-03-13	3600
Sextans-c14	10:10:05.8	-01:35:00.5	2019-03-13	3600
Sextans-c15	10:07:34.0	-02:00:09.4	2019-03-13	3600
Sextans-c16	10:03:43.9	-02:52:02.5	2019-03-14	3600
Sextans-c17	10:18:45.0	-01:11:29.8	2019-03-14	3600
Sextans-c18	10:10:07.0	-02:58:20.5	2019-03-15	3600
Sextans-c19	10:16:47.7	-00:35:26.4	2019-03-14	3600
Sextans-c1	10:13:44.5	-01:37:44.7	2019-03-11	3600
Sextans-c20	10:18:00.0	-02:15:00.1	2019-03-15	3600
Sextans-c21	10:13:58.1	-03:18:39.6	2019-03-14	3600
Sextans-c22	10:13:06.7	-00:02:55.5	2019-03-15	3600
Sextans-c23	10:22:36.2	-00:41:35.7	2019-03-15	3600
Sextans-c24	10:15:07.2	-01:52:26.0	2019-03-14	3600
Sextans-c25	10:15:27.3	-01:13:54.1	2019-03-15	3600
Sextans-c2	10:14:56.8	-01:37:11.3	2019-03-11	3600
Sextans-c3	10:16:13.0	-01:38:34.5	2019-03-11	3600
Sextans-c4	10:11:33.0	-01:50:09.1	2019-03-11	3600
Sextans-c5	10:12:48.0	-02:21:12.4	2019-03-11	3600
Sextans-c6	10:12:09.1	-01:17:05.7	2019-03-11	3600
Sextans-c7	10:13:42.9	-01:13:40.4	2019-03-12	3600
Sextans-c8	10:14:24.5	-00:42:25.4	2019-03-12	3600
Sextans-c9	10:11:00.2	-02:09:30.2	2019-03-13	3600

An additional dataset in the literature is the MMFS data collected by Walker et al. (2007, 2009). These spectroscopic observations cover the wavelength region 5140−5180 Å with a resolving power $R \sim 20,000$ containing the Magnesium triplet absorption lines. The observations were carried out between 2004 and 2009 and comprise a total of 1487 spectra. After combining results for duplicate targets the sample consists of 947 targets with median line-of-sight velocity error of 1.95 km s^{-1}. Equivalent widths for the MgT lines were used to obtain metallicities using the calibration developed by Carretta and Gratton (1997). This scaling relation was tested for metallicities between −2.24 and −0.51 dex, yielding typical uncertainties of $\sim 0.2-0.3$ dex. These metallicities are clearly not as precise as the CaT derived metallicities, thus it will be applied secondary to the FLAMES data. The footprint of this dataset is presented in the right-hand panel of Figure 2.1.

To assess the compatibility of the FLAMES and MMFS samples, overlapping targets were used to inspect the comparability of both the line-of-sight velocities as well as the metallicities. There are 242 overlapping targets with measured line-of-sight velocities of which 78 have metallicities in both datasets. The comparison between the velocities and metallicities is presented in Figure 2.2 along with a 1:1 line and a best fitting relation between the datasets. Despite some obvious differences, the radial velocities agree very well (left panel of Figure 2.2). The best fitting relation shows a very slight deviation from a 1:1 correlation, though it is well within one standard deviation. Thus it is safe to use the two samples together.

Turning attention to the metallicities derived using the different tracers in the right-hand panel of

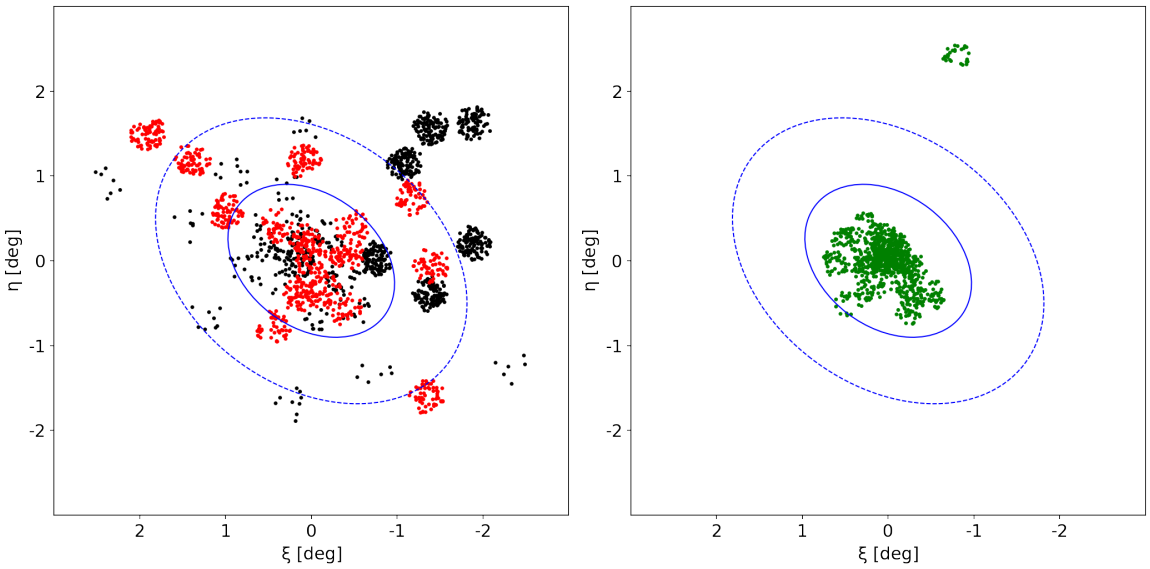

FIGURE 2.1: **Left panel:** Spatial distribution of the FLAMES spectroscopic dataset. Red targets are observed in the initial observations, black targets are observed in the 2019 run. **Right panel:** Extent of the MMFS data. The blue ellipses give the three half-light radius mark (solid), and the tidal radius (dashed), from Cicuéndez et al. (2018).

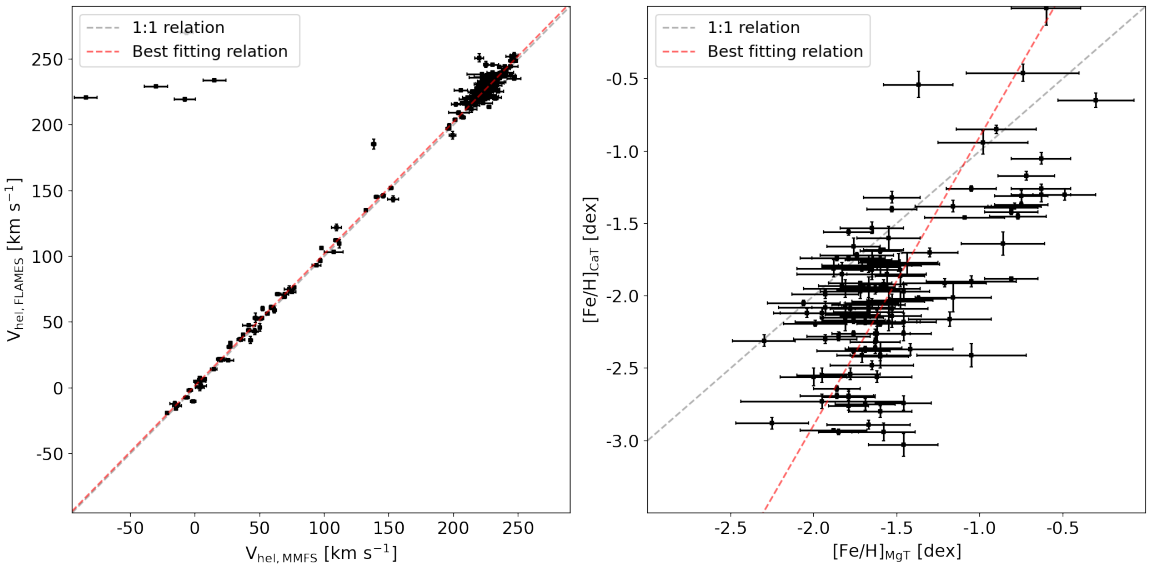

FIGURE 2.2: **Left panel:** Comparison between radial velocities determined from MMFS observations versus those obtained using FLAMES spectra. A 1:1 relation is shown in grey while the best fitting relation is presented in red. **Right panel:** Comparison between the metallicities derived from the two different tracers, Magnesium triplet for MMFS observations versus Calcium triplet for the FLAMES observations. Again a 1:1 relation with no offset is presented in grey while a best fitting relation is shown in red.

Figure 2.2 it is obvious that large differences exist: disagreements of 1 dex are not uncommon and discrepancies can get as large as 1.5 dex for extremely metal-poor stars as determined from the CaT observations. The large differences at these low metallicities come as no surprise as the calibration of Carretta and Gratton (1997) was only tested down to -2.24 dex. Since low metallicities are expected in Sextans and the values derived using the CaT calibration yield much smaller uncertainties, the MgT metallicities are discarded.

After combining the two samples a total of 2523 stars were observed for which reliable radial velocities

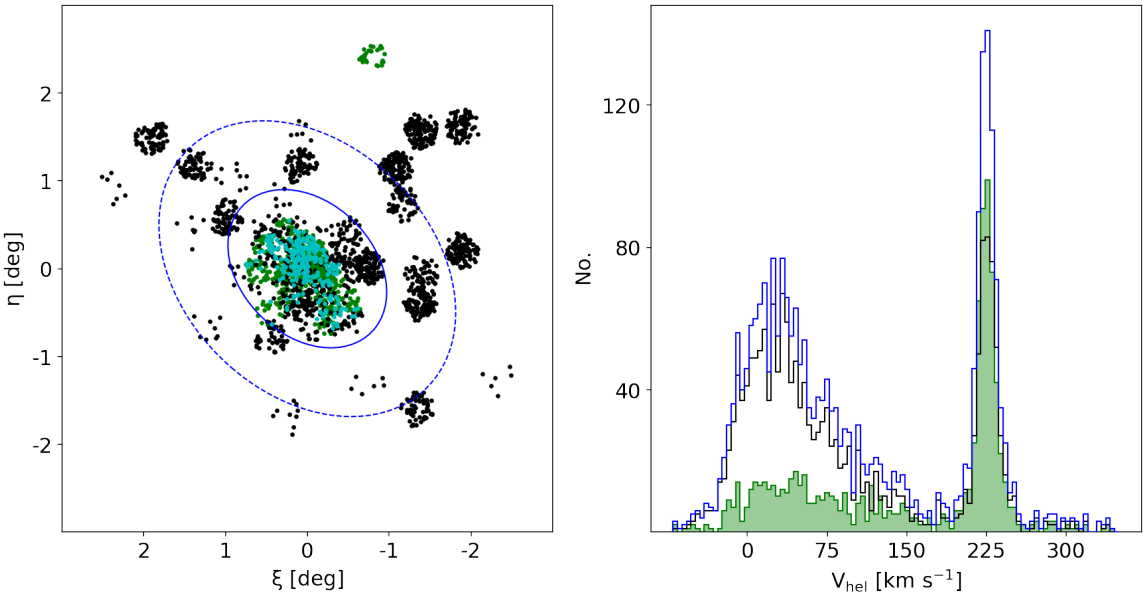

FIGURE 2.3: **Left panel:** Combined footprint of the two low resolution spectroscopic surveys. The black dots represent the FLAMES data, green the MMFS data, and the cyan points the overlapping stars between the two datasets. **Right panel:** Distribution of the heliocentric line-of-sight velocities of the combined spectroscopic sample. The black histogram shows the contribution from the FLAMES dataset, green the MMFS dataset, and blue the combined distribution. Due to the overlap between the samples this is not simply the sum of the two individual distributions.

have been determined (median uncertainty of 0.96 km s^{-1}). For 1840 of these stars reliable metallicities from the CaT lines have been determined (the FLAMES subsample, median metallicity uncertainty 0.02 dex). The spatial footprint of the combined dataset is presented in the left-hand panel of Figure 2.3. Even though the spatial coverage was significantly improved with the 2019 run of VLT/FLAMES observations, the coverage beyond 3 half-light radii remains sparse. The histogram in the right-hand panel of Figure 2.3 shows the distribution of the heliocentric line-of-sight velocities of the combined spectroscopic dataset. Clearly many stars with velocities significantly different from the systemic velocity have been observed which are contamination.

2.2 High Resolution Spectroscopy

High resolution spectroscopy provide detailed chemical abundances of a small number of stars. These abundances can be used to get insight into the chemical enrichment of a galaxy and its star formation history as well as the epoch of onset of different supernovae types with different chemical yields. The high resolution spectroscopy sample used in this thesis also consists of two parts: the first part is obtained from the literature, in particular FLAMES high resolution observations (Theler et al., 2020), while the second part consists of archival UVES (Ultraviolet and Visual Echelle Spectrograph) spectra that are processed using a pipeline I developed based on the iSpec package (Blanco-Cuaresma et al., 2014; Blanco-Cuaresma, 2019).

The sample of Theler et al. (2020) consists of 87 high resolution FLAMES/GIRAFFE spectra using the HR10, HR13, and HR14 gratings covering the wavelength range between 5340 and 6700 Å. Chemical abundances for 10 different elements have been determined, including the alpha elements magnesium, calcium, and titanium, as well as the Iron peak elements cobalt and nickel, and neutron-capture elements barium and europium. While this sample is of very high quality and includes a sizeable number of stars (87 in total), its spatial coverage is limited to only the central 25 arcminutes.

To extend the spatial coverage of the high resolution sample, archival UVES data in the direction of Sextans is explored. These spectra found in the archive are used to derive abundances for the alpha

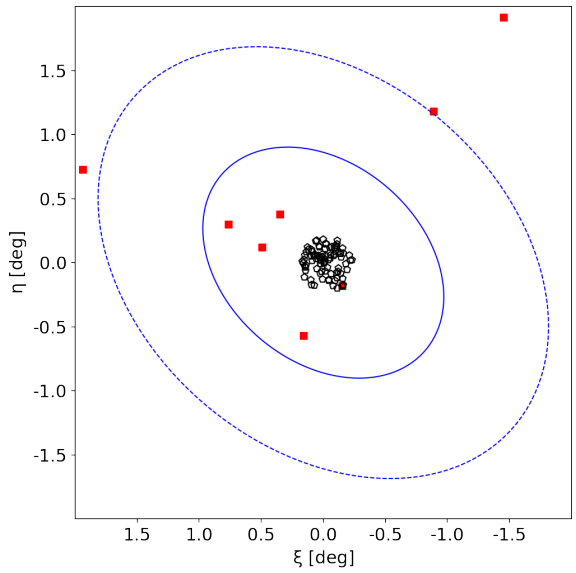

FIGURE 2.4: Spatial extent of the combined high resolution spectroscopy sample. The black open pentagons represent the data collected by Theler et al. (2020) while the red filled squares are the UVES spectra processed with the pipeline described in Section 3.1. As in Figure 2.1 the blue ellipses show the three half-light radii mark and the tidal radius of Sextans.

elements, Iron-peak elements and some neutron-capture elements including Barium and Europium. The spectra were required to have a minimum exposure time of 600 seconds and an average signal-to-noise ratio of 10. In total 32 spectra comply with these criteria in a 4 degree search radius on the central position of Sextans. These spectra are processed using a self-developed pipeline which will be described in Section 3.1. The footprint of the high resolution spectroscopy is shown in Figure 2.4. This effort extends the spatial coverage significantly compared to Theler et al. (2020).

2.3 Photometry and Astrometry

The final part of the data complements the chemical and radial velocity information from spectroscopy with accurate astrometry and photometry from the GAIA mission. This data will mainly be used to obtain robust and reliable membership probabilities for the spectroscopic targets. However, it can also be used in building a three dimensional kinematic map of the Sextans dSph, and study its velocity ellipsoid.

GAIA EDR3 data is retrieved from the archive in a circle centred on Sextans with a 6 degree radius. Only stars with a full astrometric solution, i.e. ASTROMETRIC_PARAMETERS_SOLVED ≥ 31, are considered and the Renormalized Unit Weight Error (RUWE) is required to be no greater than 1.4 to ensure the quality of the observations. Unresolved and extended objects are removed by requiring targets to have IPD_FRAC_MULTI_PEAK ≤ 2 as well as IDF_GOF_HARMONIC_AMPLITUDE < 0.2. No parallax cuts are applied since the measurement uncertainties are large, especially on the faintest stars in Sextans, meaning they can still be members even though their parallax at face-value would exclude them.

The Apparent G-band magnitudes for all 6-parameter solution sources were corrected using the Python code provided by Gaia Collaboration et al. (2021). Corrections due to dust extinction were applied using the maps of Schlegel et al. (1998) and coefficients of Marigo et al. (2008) for the GAIA filters based on Evans et al. (2018). This processing step is identical to what is employed in Sestito et al. (2019) and Battaglia et al. (2022). After this magnitude correction, the spatial coverage is trimmed to a square box with sidelengths of 6 degrees such that the spectroscopic footprint is covered. The CMD of the GAIA sample is presented in Figure 2.5 with spectroscopic targets clearly indicated.

Targets in the spectroscopic sample are crossmatched with the GAIA catalogue based on their position.

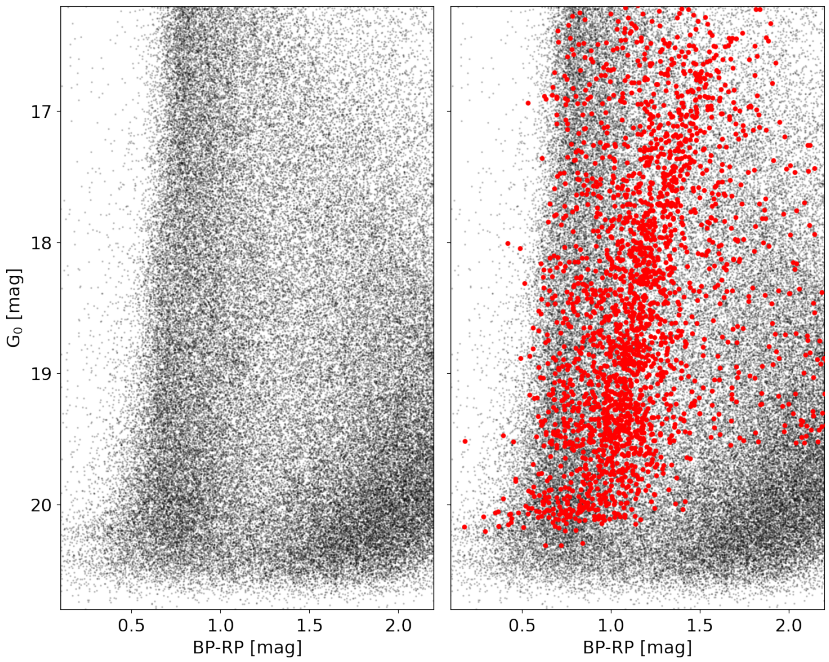

FIGURE 2.5: **Left panel:** Footprint of the GAIA catalogue in colour-magnitude space. **Right panel:** All spectroscopic targets plotted in red on top of the GAIA data.

Stars were required to be within at least 1 arcsec to be eligible for a crossmatch. Even though no quality cuts, other than the selection on RUWE, were imposed on the GAIA data, some spectroscopic targets had no match in the GAIA catalogue. The final crossmatched sample consists of 2388 distinct stars with radial velocities measured of which 1774 also have metallicities derived from the Calcium triplet in the FLAMES dataset.

Chapter 3

Data Analysis

In order to use the high resolution spectra from the UVES archive, it was necessary to reduce and analyse them. For this reason I developed pipeline to determine the atmospheric parameters and derive the chemical abundances. Membership also need to be determined for the stars. These two important processing steps will be described in the following sections, respectively.

3.1 High Resolution Spectroscopy

Fully developing a pipeline to reduce spectra from scratch in a consistent manner can take a considerable amount of time and resources. Many choices need to be made concerning optimization towards specific types of stars or treating spectra from a specific instrument. To ease the development, the pipeline designed here heavily relies on iSpec: an integrated spectroscopic framework implemented in Python (Blanco-Cuaresma et al., 2014; Blanco-Cuaresma, 2019). iSpec works in conjunction with several spectral synthesis/radiative transfer libraries such as SPECTRUM, Turbospectrum, and MOOG. The design choices made to reduce the available spectra are outlined in the following subsection as well as a comparison of the obtained results with previously published results.

3.1.1 Designing a Spectroscopy Pipeline

In order to determine atmospheric parameters and abundances the raw spectra need to be corrected for a heliocentric velocity shift. Radial velocity determinations can be done in two ways using iSpec: using a mask and atomic data or using a template. Tests were performed to find differences in the results, no significant discrepancies were found. Typically the two different methods were within $0.5\,\mathrm{km\ s^{-1}}$ of each other and always agreed within 1 sigma. Since the template method was computationally less expensive, i.e. less execution time, it was chosen over the mask method.

After the radial velocity correction, the telluric line regions were cleaned using a synthetic Telluric linelist that comes with iSpec. Next the spectrum is normalized in a two step manner. First a median filter with a wavelength range of 0.1 nm is applied followed by a maximum filter with a wavelength step of 1 nm. These are in place to reduce noise effects and avoid normalizing absorption lines when estimating the continuum. After this splines are fitted to estimate the continuum level. These splines have a degree of 2 (the recommended default in iSpec) and one spline is constructed for every window of 5 nm. Finally any cosmic ray hits and remaining negative fluxes are removed to have a fully cleaned spectrum for atmospheric parameter and abundance estimations.

For the atmospheric parameters and abundance estimation, a line mask is constructed. To proceed with this step a linelist is needed, which was taken from Hill et al. (2019) with updated atomic data from the VALD-3 database (Ryabchikova et al., 2015; Pakhomov et al., 2019). MARCS model atmospheres are used (Gustafsson et al., 2008) since we are dealing with red giant branch (RGB) stars. For the spectral synthesis the MOOG library is used (Sneden, 1973; Sneden et al., 2012). Moog

TABLE 3.1: Stellar parameters derived using our pipeline compared to previously published results. All literature abundances are on the scale of Asplund et al. (2009).

	Developed Pipeline				Literature					
Name	T_{eff} [K]	log g [dex]	[Fe/H] [dex]	[Mg/Fe] [dex]	T_{eff} [K]	log g [dex]	[Fe/H] [dex]	[Mg/Fe] [dex]	Instrument	Reference
S24-72	4340	0.83	-2.76	0.19	4340	0.74	-2.90	0.18	HDS	Aoki et al. (2020)
S11-04	4330	0.69	-2.55	0.15	4230	0.62	-2.85	0.28	HDS	Aoki et al. (2020)
S04-130	4470	1.11	-2.49	0.14	4520	1.07	-2.94	0.45	UVES	Lucchesi et al. (2020)
S11-97	4450	0.96	-2.55	0.15	4480	1.10	-3.01	0.49	UVES	Lucchesi et al. (2020)

was chosen for efficiency as it does not fully synthesize each line individually, like SPECTRUM or Turbospectrum do, bu rather uses a direct computation technique. The atmospheric parameters to be determined are: effective temperature, surface gravity, metallicity, alpha enhancement and micro- and macro-turbulence velocities. Which are estimated first and fixed when deriving chemical abundances. The chemical abundances are determined on a line-by-line basis. For elements with multiple lines a weighted average of the individual estimations is used as the final abundance, of course discarding lines for which no reliable abundance could be determined. After the abundance calculations, all abundances are put on a solar scale from Asplund et al. (2009) to derive [X/Fe] values.

3.1.2 Results of the Spectroscopy Pipeline

Out of the 32 spectra retrieved from the ESO archive, the pipeline was not able to derive a full atmospheric parameter solution for 8 of these. All 8 spectra had the minimum exposure time of 600 seconds, and a signal-to-noise ratio around 20. These spectra looked more noisy than other spectra with similar signal-to-noise ratios and longer exposure times. Concluding: out of the 32 input spectra, 24 spectra have a full atmospheric parameter solution. The median uncertainty on the derived effective temperature is 140 K, while the median uncertainty on the surface gravity is 0.6 dex. These uncertainties are mainly driven by the relatively low signal-to-noise ratios for the spectra.

After combining the results for stars with multiple observations, the final sample consists of 8 individual targets. This operation also drastically reduced the median uncertainties on the effective temperature and surface gravity to 55 K and 0.25 dex, respectively. Out of these 8 stars, four have stellar parameters that are consistent with being RGB stars. For these 4 stars we compare their derived parameters with published values. This comparison can be found in Table 3.1, these four stars are also confirmed to be high probability members of Sextans while the other four are considered to be contamination. From this comparison it is evident that the developed pipeline performs well when determining the effective temperature and the surface gravity, but overestimates the metallicities of the stars by several tenths of a dex in the worst case. It should be noted that the effective temperatures in the literature were determined using photometry while the surface gravities have been derived using a relation with the effective temperature, mass, and bolometric magnitude. In our pipeline the effective temperature and surface gravity are both determined directly from the spectra. They are very comparable to one-another, though the uncertainties on the spectroscopically determined parameters are significantly larger. Differences between the relative magnesium abundances are smaller but still significant, but can be the effect of overestimating the iron abundance. The differences can arise from many different components, likely related to specific choices that were made when designing the pipeline. However, the general similarity of the results gives confidence that our pipeline can be used for the reliably.

3.2 Membership Determination

A recurring issue in detailed studies of dwarf galaxies is how to determine which star is actually part of the dwarf galaxy in question and which is Milky Way contamination. Customarily this was done using hard cuts in colour-magnitude space along with $k\sigma$-clipping in radial velocity space (3σ selections around the systemic velocity are typically used). However, these methods will always risk

including stars that are contamination and excluding stars that are highly likely to be members in different parameter spaces like proper motion space. With the advent of GAIA and the exquisite astro- and photometry it provides, novel Bayesian techniques have been developed that yield very robust membership probabilities even in the very diffuse outskirts of dwarf galaxies (Pace and Li, 2019; McConnachie and Venn, 2020a; Battaglia et al., 2022). These methods never used radial velocity information from spectroscopy, which has the potential to be a very strong membership discriminator.

Pace and Li (2019) started their method with the idea that every star in a catalogue can be described using a mixture of stars that are either part of Sextans or part of the Milky Way contamination and define the total likelihood for a single star as

$$\mathcal{L} = f_{\rm sat}\mathcal{L}_{\rm sat} + (1 - f_{\rm sat})\mathcal{L}_{\rm MW} \tag{3.1}$$

in which $\mathcal{L}_{\rm sat}$ and $\mathcal{L}_{\rm MW}$ are the likelihoods for the star to be part of the satellite, i.e. Sextans in this case, and the Milky Way, respectively. $f_{\rm sat}$ is the approximate fraction of stars in the catalogue that are part of the satellite and acts as a normalization for the total likelihood. The likelihood of the full catalogue is then the product of the likelihoods for all the individual stars since the measurements are independent. Both likelihood terms can be broken into four constituents representing the different parameter spaces to be considered

$$\mathcal{L}_{\rm sat/MW} = \mathcal{L}_{SP}\mathcal{L}_{CM}\mathcal{L}_{PM}\mathcal{L}_{RV} \tag{3.2}$$

where the individual terms incorporate the spatial likelihood, colour-magnitude space, proper motion likelihood, and the radial velocity information, respectively. The inclusion of the colour-magnitude information has been done before (McConnachie and Venn, 2020a; Battaglia et al., 2022) but the addition of radial velocity measurements has not been done before since large spectroscopic datasets are not always available. For the spatial, colour-magnitude and proper motion likelihood components, two dimensional lookup tables were constructed and all normalized to unity while for the radial velocity a one dimensional version suffices.

The spatial likelihood of a star depends on the stellar density of Sextans compared to the Milky Way contamination. Structural parameters are needed to describe the stellar density using a simple two dimensional Plummer profile. The structural parameters from Cicuéndez et al. (2018) are used and listed in Table 3.2. To take into account the uncertainties on the structural parameters, 1000 synthetic realizations of the spatial likelihood were constructed with structural parameters drawn from Gaussian distributions centred on the reported values with a standard deviation equal to the measurement uncertainty. The synthetic realizations were coadded before normalizing the whole likelihood to unity. Figure 3.1 shows the final spatial likelihood map as well as the impact of incorporating the uncertainties on the structural parameters.

The Milky Way contamination is modelled using a spatially uni- form likelihood map, i.e. the stellar density from the contamination is expected to be the same everywhere. While this is not necessarily true since Sextans is close to the Galactic disk and a gradient in the stellar density can be expected, this variation is hard to model and is not expected to change the results in a meaningful way. Another possibility resulting in non-uniformity is the presence of substructures like stellar streams in the vicinity of Sextans. However, the impact of these structures is impossible to model if they are not known. Moreover, coherent substructures with a distinct radial velocity are expected to be filtered out by including the radial velocity information.

TABLE 3.2: Structural parameters used to construct the spatial likelihood lookup table. All parameters come from Cicuéndez et al. (2018).

R.A. [deg]	Decl. [deg]	θ [deg]	r_h [arcmin]	$e = 1 - b/a$
153.268	-1.618	52 ± 3	21.4 ± 0.7	0.27 ± 0.03

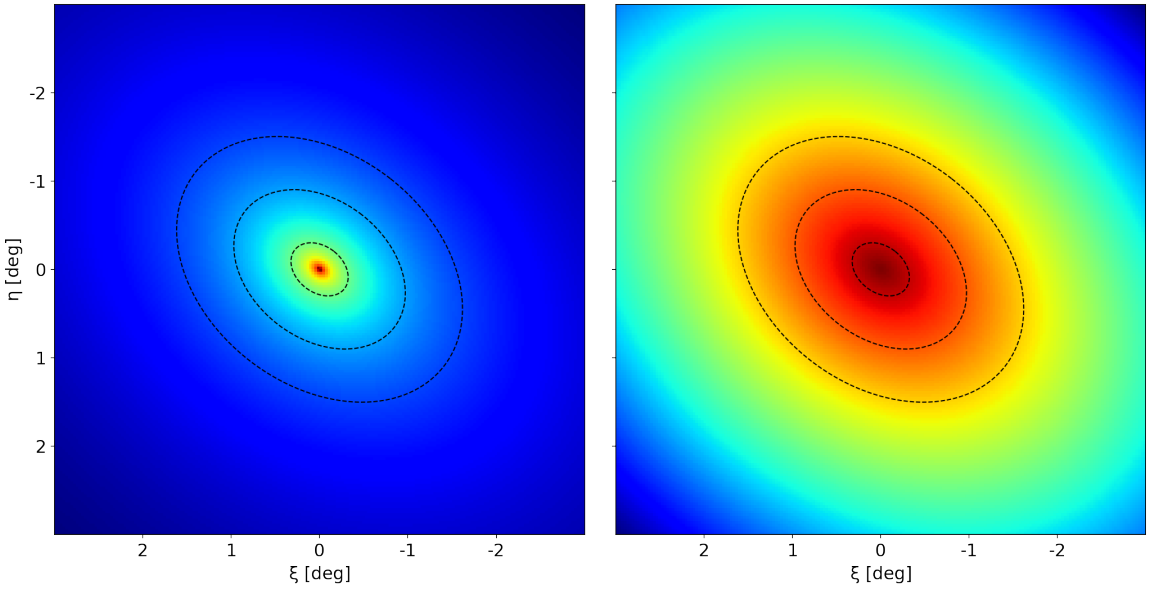

FIGURE 3.1: **Left panel:** Spatial likelihood map without taking into account the uncertainties on the structural parameters. **Right panel:** Identical to the right panel but now the uncertainties on the structural parameters are considered. Both panels have identical logarithmic scalings. The dotted black ellipses give the one, three, and five half-light radii, respectively.

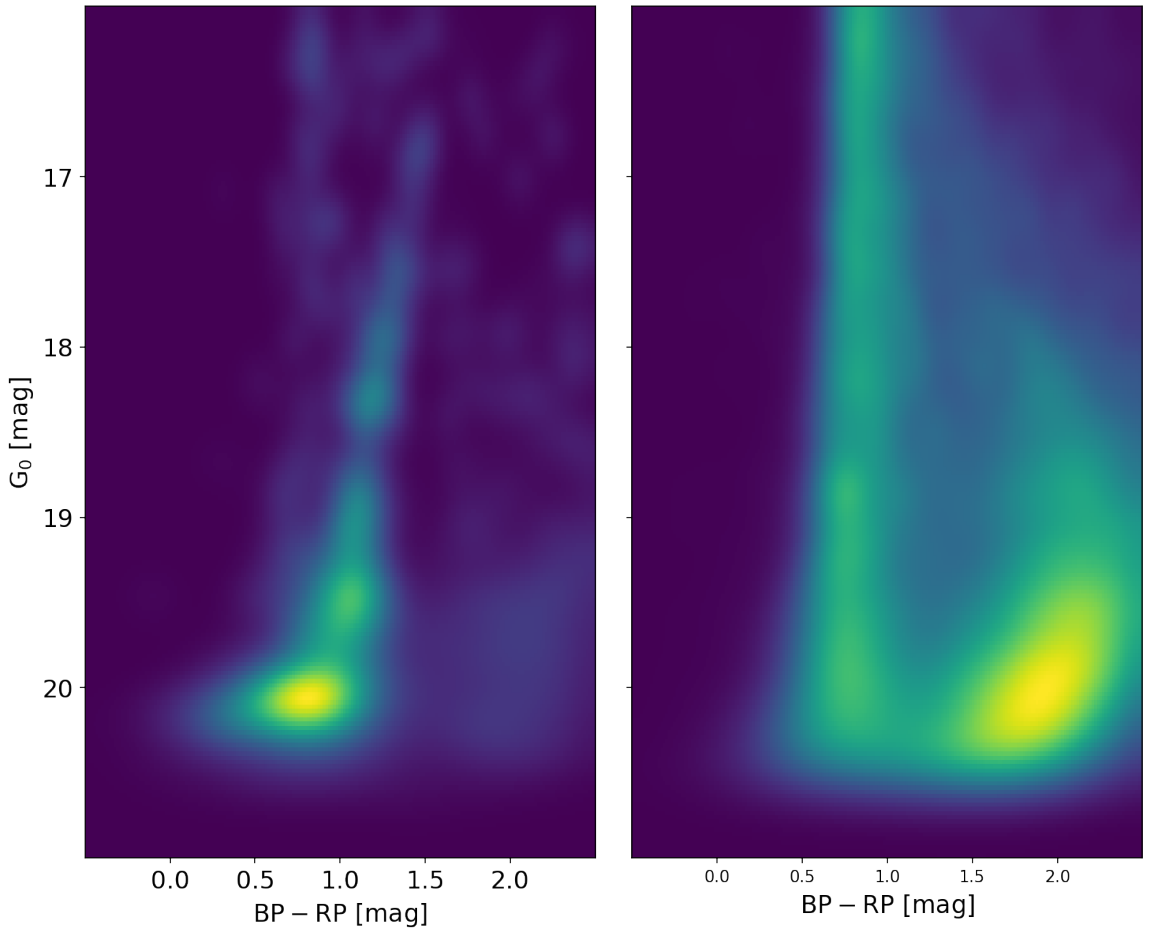

FIGURE 3.2: **Left panel:** CM space likelihood for stars expected to be members of Sextans. **Right panel:** Identical as the right panel but for stars that are expected to be contamination. Both panels have linear scaling.

The construction of the colour-magnitude likelihood is inspired by Battaglia et al. (2022): assuming Sextans is a well populated system in the GAIA catalogue, the colour-magnitude likelihood maps can be determined completely using the data at hand. This holds both for the member stars and the Milky Way contamination.

The likelihood distribution on the colour-magnitude plane for member stars is determined from all stars within in a single half-light radius, as the stellar population of Sextans is expected to dominate over the contamination in that region. The CMD is constructed by modelling each star as a two-dimensional Gaussian in colour-magnitude space centred on the measurement values with standard deviations given by the measurement uncertainties. The distribution is calculated on a grid ranging from $-0.5-$ 2.5 mag in the colour direction and G- magnitudes ranging from $21-$ 16 mag with 200 'pixels' in each direction. The CM plane of individual stars is coadded to obtain the full colour-magnitude distribution. After inspection, the CMD appeared very patchy: a structure resembling an isochrone was present, though it had holes and was rather narrow. To remedy both of these issues a smoothing filter was applied by convolving the CMD with a Gaussian filter with a 5 pixel smoothing kernel.

To construct the colour-magnitude likelihood distribution for the Milky Way contamination a similar approach is followed. However, instead of considering stars within one half light radius, only stars outside five half-light radii are used. It is expected that beyond 5 half-light radii the contamination will be the dominant factor in the stellar density. The rest of the procedure is identical to what has been done for the member star CMD: model each star as a 2D Gaussian in CM space, coadd the individual CM planes, convolve the obtained distribution with a Gaussian smoothing kernel and normalize to unity. Both likelihood maps are presented in Figure 3.2.

To build a model for the proper motion of member stars, they are assumed to all share the same systemic proper motion $(\mu_\alpha \cos\delta,\ \mu_\delta)$. The spread of individual proper motions is assumed to be completely due to measurement uncertainties, as they will dominate over any intrinsic proper motion dispersion. The proper motion likelihood is then described using a bivariate Gaussian distribution centred on the systemic proper motion with a covariance matrix given by the measurement uncertainties on the individual components and their correlation. The systemic proper motion is thus a parameter that needs to be estimated using the data at hand.

The Milky Way contamination in proper motion space is modelled using a similar method to the one used for the CM space. All stars in the GAIA catalogue more than five half-light radii from the centre are considered. They are modelled as a bivariate Gaussian in proper motion space using the measured values with their uncertainties and correlation. Individual planes are coadded before normalizing the obtained likelihood table. Contrary to the CM case, no smoothing filter needs to be applied. The likelihood map is calculated on a grid ranging from $-10 - +\ 10$ mas yr^{-1} in both directions, corresponding to a tangential velocity of ~ 1000 km s^{-1} at the distance of Sextans, in order to ensure a full exploration of the proper motion space. The final proper motion likelihood map is presented in Figure 3.3.

The radial velocity likelihood for member stars is similar to the one for proper motions, instead of using a two dimensional Gaussian, a univariate version suffices. However, in this case the intrinsic velocity dispersion will contribute significantly since it is relatively large compared to the measurement uncertainties. This gives two more parameters that need to be estimated: the heliocentric radial velocity $V_{\rm hel}$ and the stellar velocity dispersion σ_V^*.

The Milky Way contamination is assumed to follow a uniform distribution in radial velocity space, much like the spatial model. Even though the bulk motion from stars in the Milky Way can be modelled, it is hard to do so properly. Contributions from coherent substructures are expected to have distinguishable radial velocities too, however these are unknown. We expect that combining the different parameter spaces will filter out any ambiguous stars that might appear in individual likelihood components.

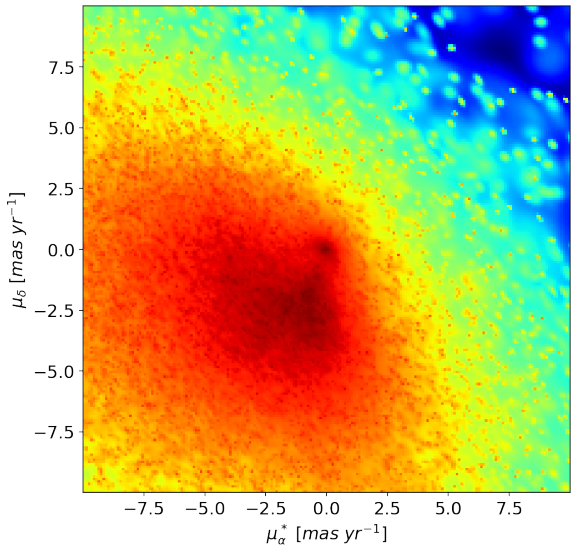

FIGURE 3.3: The proper motion likelihood map constructed for the Milky Way contamination, shown with logarithmic scaling.

TABLE 3.3: **Prior:** Parameters used to calculate the prior distributions for the parameters to be estimated. Proper motion data comes from McConnachie and Venn (2020a), radial velocity and velocity dispersion from Battaglia et al. (2011). **Posterior:** Maximum a-posteriori estimates of the model parameters after evaluating the posterior distribution with PyMC3.

	$f_{\rm sat}$	$\mu_\alpha \cos\delta$ (mas yr^{-1})	μ_δ (mas yr^{-1})	$V_{\rm hel}$ (km s^{-1})	σ_V^* (km s^{-1})
Prior	$[0, 1]$	-0.44 ± 0.02	0.08 ± 0.02	226.0 ± 0.6	8.4 ± 0.4
Posterior	0.27 ± 0.01	-0.41 ± 0.01	0.03 ± 0.01	225.9 ± 0.4	6.4 ± 0.2

In a Bayesian framework, the probability of obtaining a dataset D under a model with parameters θ is given by the posterior distribution

$$P(D|\theta) = \mathcal{L}(\theta|D)P(\theta) \tag{3.3}$$

in which the dependence of the likelihood on the data and the model parameters has been made explicit. $P(\theta)$ is the prior distribution of the model parameters and incorporates any previous information as well as constraints on the model parameters. Given the previously described likelihoods, there are five parameters that need to be estimated: the fraction of stars in Sextans, $f_{\rm sat}$, and the four parameters concerning the systemic motion, $\mu_\alpha \cos\delta$, μ_δ, $V_{\rm hel}$, and σ_V^*. Once these parameters that optimize the posterior $P(D|\theta)$ are known, the individual likelihoods can be calculated and the membership probability for individual stars can be found using

$$P_{\rm mem} = \frac{f_{\rm sat}\mathcal{L}_{\rm sat}}{f_{\rm sat}\mathcal{L}_{\rm sat} + (1 - f_{\rm sat})\mathcal{L}_{\rm MW}} \tag{3.4}$$

For the priors concerning the systemic motion, Gaussian distributions are adopted centred on the values reported in Table 3.3 with standard deviations given by the uncertainties on the reported values. Since the uncertainties on the proper motion components are very small, possibly making the prior too restrictive, the uncertainties were multiplied by 5 to ensure the full proper motion parameter space is explored properly. Furthermore, the prior distribution on the velocity dispersion has a cut-off imposed at zero as a negative velocity dispersion is nonsensical. The impact of the priors was tested by shifting around the centres and varying the width of the distributions, however, no significant impact on the final results was found.

To explore the parameter space PyMC3 was used (Salvatier et al., 2016), an open-source Hamiltonian Monte Carlo package implemented in Python. The maximum a-posteriori estimates for the model

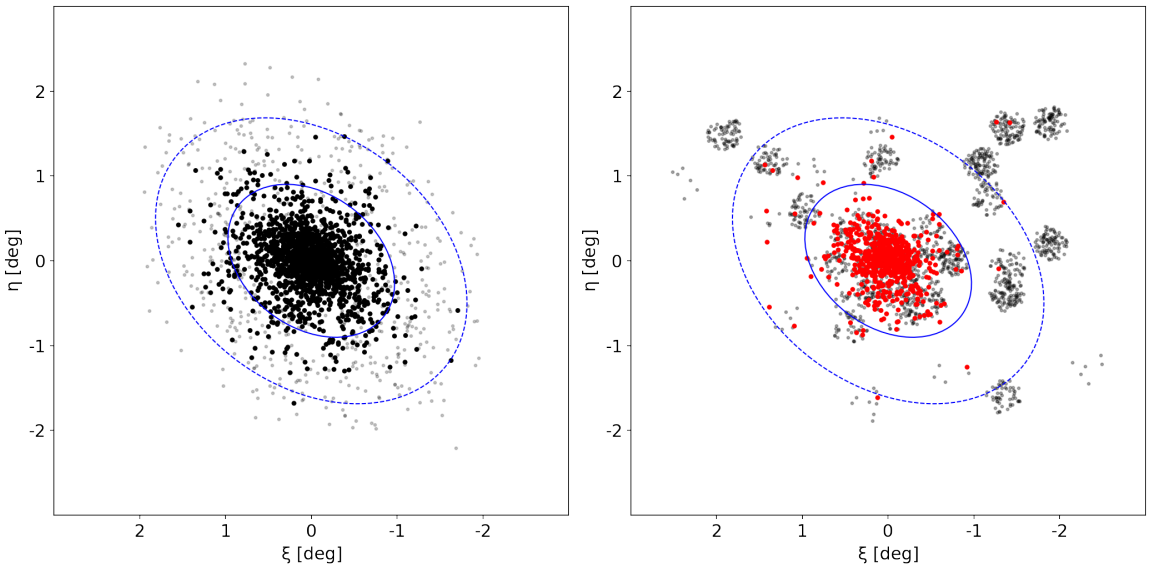

FIGURE 3.4: **Left panel:** Spatial distribution of all possible members of Sextans included in the GAIA catalogue. The small grey dots are stars with membership probability between 0.1 and 0.5 which could be interesting for spectroscopic observations. **Right panel:** Footprint of the spectroscopic observations, red points are stars with high membership probabilities while small grey dots represent non-members. Again the blue ellipses give the three half-light radii and tidal radius mark, as in Figure 2.1.

parameters are listed in Table 3.3. The proper motions agree with McConnachie and Venn (2020b), this is expected as the same data is used. The systemic radial velocity is in agreement with literature values, though the velocity dispersion is significantly lower than literature values (6.4 ± 0.2 km s^{-1} is found compared to 8.4 ± 0.4 km s^{-1} in Battaglia et al. (2011)). After fitting the radial velocity and velocity dispersion again, only considering stars that came out as members in this analysis, a velocity dispersion of 8.7 ± 0.3 km s^{-1} was found agreeing with literature.

After calculating the membership probabilities using Equation 3.4 and requiring $P_{\rm mem} \geq 0.5$ for stars to be a member of Sextans, the member sample is constructed. Out of the 2388 total spectroscopic targets with matches in the GAIA data, 644 stars were found to be high probability members of Sextans (mean membership probability of 0.998). All of these stars have measured radial velocities and a subset of 556 have Calcium triplet metallicities. The mean membership probability was also calculated when radial velocities were not considered, which left a few ambiguous stars. However, this ambiguity was lifted by the inclusion of radial velocities. Moreover, for stars that were already clearly members or non-members, the radial velocity confirmed this. Hence we can be sure that the membership probabilities are robust. The membership criteria brings the number of targets in the high resolution spectroscopy to a total of 82 members. Four of these are observed with UVES and reduced with the developed pipeline while the other 78 come from Theler et al. (2020).

The difference between all the possible members in the full GAIA catalogue and those that are included in the spectroscopic dataset is presented in Figure 3.4. From the current selection in the GAIA data there are over 1600 members of Sextans in the catalogue. It becomes very clear that beyond three half-light radii the sampling of the spectroscopy is sparse because members are also spare. This also results in many stars that were observed beyond three half-light radii to be non-members, courtesy of the rough selection criteria employed especially in the early target selection. Selecting targets for spectroscopic studies is a difficult process as you do not want to exclude obvious members but also maximize the efficiency of observation time by selecting as many members as possible per field. Traditionally the target selection has been done based on CMD position, selecting a wide area around the red giant branch of the system. However, with GAIA a very targeted selection of members can be made. Even when relaxing the constraint of membership, to for example $P_{\rm mem} \geq 0.1$ resulting in

just over 2300 possible members for which GAIA data is available, observations can be made more efficient and the radial velocities can be the deciding factor in the final membership. With upcoming instruments like WEAVE and 4MOST (Dalton et al., 2018; de Jong et al., 2019) these numbers of targets should be observable as well, leading to better sampling of the system to larger distances.

Chapter 4

Kinematic Results

Before diving head first into the full capabilities of the dataset at hand, it is important to revisit previously published results. This is to check for consistency with previous research and see if any systemic differences are introduced before moving on to the new possibilities of the current data.

Previous detailed studies of dwarf spheroidals using large spectroscopic datasets with hundreds of line-of-sight velocities revealed the presence of velocity gradients in several of them, including Sextans (Battaglia et al., 2009, 2011; Hermosa Muñoz et al., 2020).

4.1 Velocity Gradient

The left panel of Figure 4.1 shows the large scale velocity distribution of Sextans. A Gaussian smoothing filter is applied with a 0.2° FWHM to reduce spurious changes due to individual velocities. From the figure it is easy to pick out a velocity gradient by eye aligning roughly with the major axis of the system. The right panel in Figure 4.1 shows a zoom-in of the central region of Sextans. Again a smoothing filter is applied with a FWHM of 5 arcmin to show smaller scale details.

To test for the presence of a velocity gradient in Sextans, a simple model is used in which velocities are considered relative to the systemic velocity of Sextans:

$$V_i = V_{\rm sys} + V_{\rm rel}(R_i, \theta_i) \tag{4.1}$$

where R_i and θ_i are the angular distance to the centre and position angle with respect to the major axis of individual stars, respectively, V_i is the measured radial velocity for the individual stars. For the relative velocity two different models responsible for the gradient were tested:

- A linear or solid-body rotation model in which the relative velocity increases linearly with distance to the centre of Sextans, i.e. $V_{\rm rel}(R_i, \theta_i) = kR_i \cos(\theta_0 - \theta_i)$ where k is a constant velocity gradient and θ_0 gives the clockwise rotation angle with respect to the major axis at which the velocity gradient exists.
- A flat or constant rotation model $V_{\rm rel}(R_i, \theta_i) = V_c \cos(\theta_0 - \theta_i)$ where θ_0 has the same meaning as in the previous model and V_c is a constant circular velocity.

After subtracting the velocity gradient, a new systemic velocity and velocity dispersion are determined to compare with a dispersion only model which has been calculated in Section 3.2, i.e. $V_{\rm GSR} = 64.30\,{\rm km\ s^{-1}}$ and $\sigma_V^* = 8.7\,{\rm km\ s^{-1}}$, respectively.

Both models require 4 parameters to be estimated, which will be determined using a maximum likelihood procedure taking into account the measurement uncertainties on the individual velocities. To quantify the impact of stars at large distances from the centre of Sextans, the models are fitted to a subsample of the data considering all stars within 3 half-light radii and a sample in which all stars are used, even those beyond the tidal radius of Sextans. Another issue to consider is the presence of

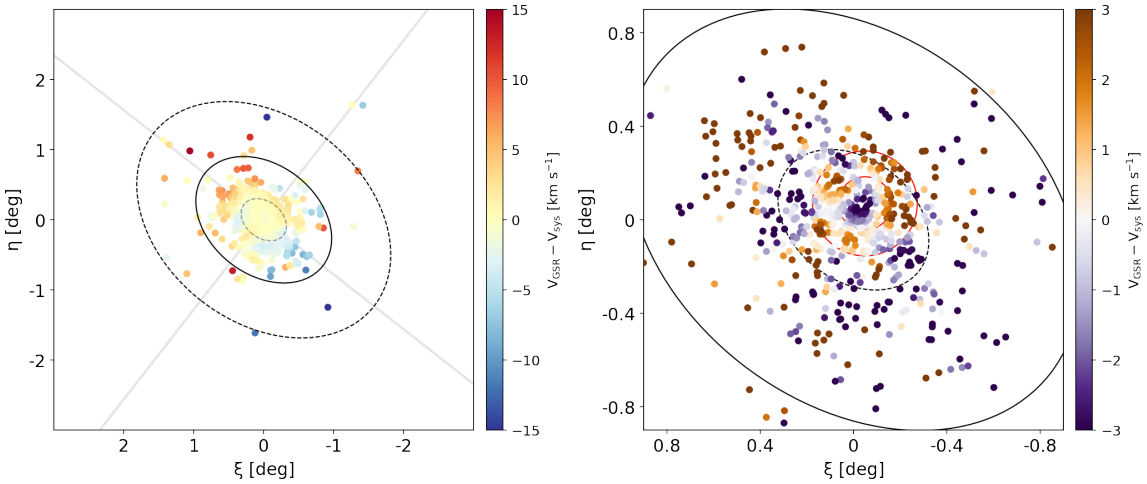

FIGURE 4.1: **Left panel:** Velocity field of the Sextans member stars. A Gaussian smoothing filter with a 0.2° FWHM is applied to make the global structure more clear. The grey axes indicate the major- and minor axis. **Right panel:** Zoom-in of the velocities in the central region of Sextans. Again a smoothing filter is applied, though this time with a 5 arcmin FWHM. A diverging colourscale is chosen in this case to highlight deviations from the systemic velocity more clearly. The ellipses show, moving outwards, the one half-light radius, three half-light radius, and tidal radius mark, respectively. Red circles roughly indicate the position of the ring-structure reported in Cicuéndez and Battaglia (2018).

small structures in Sextans, like the ring-structure, and their impact on the current analysis of the large scale velocity gradient. To 'remove' the signal from these structures, fits in which a Gaussian smoothing filter is applied will also be performed with different smoothing lengths.

The results of this fitting procedure are summarized in Table 4.1. The significance column is calculated using a bootstrapping procedure in which a velocity measurement is randomly re-assigned to a position R_i, θ_i before calculating the velocity gradient k or V_c again while keeping the angle θ_0 fixed. This is repeated for 20,000 iterations after which a frequency is calculating representing the number of times the reshuffled mock data produces a velocity gradient magnitude that is equal to or larger than the maximum likelihood estimate.

Given that all tested models return a velocity gradient that is rarely found in the mock datasets during the bootstrapping procedure, we can be confident that the gradient is real. Interestingly, in none of the cases does subtracting the velocity gradient result in a decrease of the velocity dispersion. In all cases the dispersion increases slightly and remains within 1 standard deviation from the dispersion without taking into account any rotation. In all tested cases, including stars beyond 3 half-light radii, this does not change the magnitude of the velocity gradient, it only affects the direction of the gradient. This can indicate that the gradient does change direction with radius but it can also very well be an effect of the non-uniform sampling of the spectroscopic data which becomes noticeable beyond $2-3$ half-light radii. The magnitude of the gradient is comparable to what was found by Battaglia et al. (2011) and consistent within one standard deviation with their gradient found along the major axis for a model in which the rotational velocity increases linearly with radius. Two differences with the previous analysis exist: all stars in the sample are used, compared to only the stars within a narrow slit around a preset axis in Battaglia et al. (2011), also the angle of the axis of the velocity gradient is left as a free parameter.

Even though the current analysis clearly indicates the presence of a large scale velocity gradient in Sextans, this does not directly lead to the conclusion that the system is wholly or partially supported by rotation. Other factors like streaming motions due to tidal interaction with the Milky Way and the perspective effect of Sextans moving along its orbit can have major contributions. No clear signs of tidal disruption such as tidal tails or S-shaped contours are found in the current data. However, it

TABLE 4.1: Results of the maximum likelihood estimates for the parameters of the velocity gradient model. The linear and flat gradient model were tested in a number of combinations of maximum elliptical radius and kernel size for smoothing of the velocities. The column $\mathrm{FWHM_{smooth}}$ gives the FWHM of the Gaussian function used to smooth the velocities, the significance column indicates the percentage of mock datasets in the bootstrapping procedure in which an amplitude of the velocity gradient was detected equal to or larger than the amplitude from the maximum likelihood procedure.

			Linear Increasing Gradient			
max $\mathrm{R_{ell}}$ $\mathrm{nR_h}$	$\mathrm{FWHM_{smooth}}$	V_{sys} [km s^{-1}]	σ_V [km s^{-1}]	k [km s^{-1} deg^{-1}]	θ_0 [deg]	Significance %
3	0	64.28 ± 0.03	9.1 ± 0.3	10.46 ± 0.08	17.5 ± 0.6	< 0.005
	$5'$	64.15 ± 0.03	9.0 ± 0.3	9.02 ± 0.07	15.5 ± 0.7	< 0.005
	$0.2°$	63.90 ± 0.03	8.9 ± 0.3	6.66 ± 0.08	17.4 ± 0.9	< 0.005
10	0	64.16 ± 0.03	9.0 ± 0.3	9.82 ± 0.07	23.8 ± 0.5	< 0.005
	$5'$	64.06 ± 0.03	8.9 ± 0.3	8.53 ± 0.07	23.6 ± 0.6	< 0.005
	$0.2°$	63.86 ± 0.03	8.9 ± 0.3	6.36 ± 0.07	23.8 ± 0.7	0.005
			Flat/Constant Gradient			
max $\mathrm{R_{ell}}$ $\mathrm{nR_h}$	$\mathrm{FWHM_{smooth}}$	V_{sys} [km s^{-1}]	σ_V [km s^{-1}]	V_c [km s^{-1}]	θ_0 [deg]	Significance %
3	0	64.33 ± 0.03	9.1 ± 0.3	3.88 ± 0.04	10.8 ± 0.7	0.005
	$5'$	64.20 ± 0.03	9.0 ± 0.3	3.30 ± 0.04	11.3 ± 0.8	< 0.005
	$0.2°$	63.94 ± 0.03	9.0 ± 0.3	2.46 ± 0.04	15.4 ± 1.1	< 0.005
10	0	64.28 ± 0.03	9.1 ± 0.3	3.89 ± 0.04	13.5 ± 0.7	< 0.005
	$5'$	64.18 ± 0.03	9.0 ± 0.3	3.31 ± 0.04	14.7 ± 0.8	< 0.005
	$0.2°$	63.95 ± 0.03	9.0 ± 0.3	2.48 ± 0.04	19.8 ± 1.1	< 0.005

must be noted that the detection of such signatures can be very difficult (Muñoz et al., 2008). Sextans being diffuse makes this job no easier. Walker et al. (2008) showed that velocity gradients can be the result of the systemic proper motion and actually use the radial velocity gradient to constrain the systemic proper motion in the case of Fornax and Carina. However, in those cases the velocity gradient exists along the minor axis of the system and roughly aligns with the proper motion vector which is not the case for Sextans. Hence it is very likely that the currently detected velocity gradient is the result of systemic rotation roughly around the minor axis of the system.

4.2 Radial Velocity Profiles

Line-of-sight velocity and velocity dispersion profiles are determined in Sextans by binning member stars and assuming that the velocities in each bin arise from a singular Gaussian distribution. The parameters of this Gaussian are determined using a Hamilotnian Mone Carlo (HMC) run to explore the parameter space. Battaglia et al., 2011 showed that different approaches to binning stars together, i.e. binning in circular or elliptical bins and binsizes, does not impact the results in any significant way, all types of binning agree with each other within standard uncertainties. Elliptical bins were chosen with a fixed width that increases with distance from the centre to account for the lower density of stars in the outskirts and to keep a statistically significant number of stars in each bin. The impact of the velocity gradient, and removing it, on the dispersion profiles is assessed, both for the linear increasing gradient and the flat gradient. The resulting profiles are presented in Figure 4.2.

Comparing the current results with Battaglia et al. (2011), it is evident that the current analysis is able to probe the profiles with better statistics and more bins while also extending the profiles much further into the outskirts of Sextans. Concerning the overall shape of the profiles themselves in the case of different rotation models, they all agree with other. This was also the case in the Battaglia et al. (2011) data, where the removal of the rotation signal did not result in significantly different

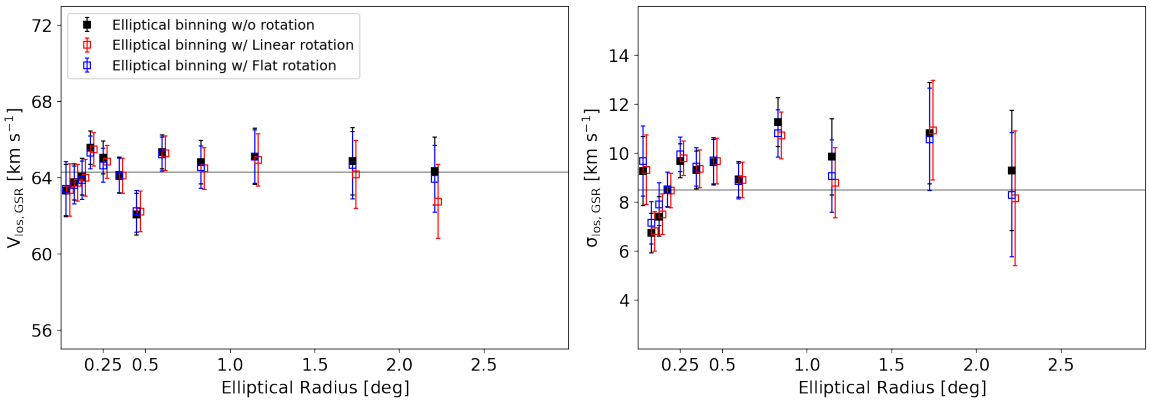

FIGURE 4.2: **Left panel:** Line-of-sight velocity in the GSR system as a function of distance to the centre of Sextans. **Right panel:** Velocity dispersion determined for the same bins as in the left panel. The black filled squares represent a pressure-only supported system while the open squares assume intrinsic rotation: red squares are for the linear increasing gradient, black squares for the flat gradient. The markers for the linear rotation model are slightly offset to the right to make their position more clear, but are calculated on the same elliptical radii as the other two models. The horizontal lines indicate the systemic velocity and systemic velocity dispersion in the left and right panel, respectively.

dispersion profiles. An interesting point is the sudden drop in line-of-sight velocity around 0.5°. this is consistent with being a remnant of a ring-structure contributing to the inwards bins. The ring is offset from the centre of Sextans and contributes to increasing the line-of-sight velocities until a radius of roughly 0.5°, resulting in a drop in the line-of-sight velocities. This is supported by the velocity dispersion at this point, which remains the same.

The shape of the velocity dispersion profile agrees with Battaglia et al. (2011), for their models that use elliptical binning, both in the case when rotation is included and excluded. Again the differences between rotation or not are very small. Interestingly is the innermost datum has a high velocity dispersion compared to the following points. Kleyna et al. (2004) found a kinematically cold substructure in the innermost region of Sextans which was hypothesized to be the relic of a stellar cluster that had migrated inwards. However, this was based on very small number statistics. This idea is not consistent with the current data. Still it remains interesting that the most central velocity dispersion datum is almost double that of the following point.

Moving further outwards, after the central rise the velocity dispersion remains roughly flat up to the outermost point. This remains the case when the velocity gradient corrected velocities are used. No significant differences arise from correcting for a velocity gradient and what kind of model is used in doing so for the datapoints beyond one degree in elliptical radius. Different from what Battaglia et al. (2011) found, when considering the velocities corrected with a linear rotation model the dispersion was found to keep rising up to the outermost datum (see the lower right panel in their Figure 12). However, this might be caused by the low number statistics especially in the bins with large distances from the centre. This is not the case in the current analysis except for the outermost bin which only has a few stars in it, resulting in the large uncertainties.

4.3 The Ring-Structure

Cicuéndez and Battaglia (2018) reported a clear kinematic substructure in Sextans appearing as a ring in the (smoothed) line-of-sight velocities. This feature is also detectable in the current dataset, and is indicated in the right-hand panel of Figure 4.1. The ring appears off-centre and rather clumpy, though it is definitely present. Stars are considered to be part of the ring-structure if their elliptical radius is within 0.5° from the centre of Sextans and their smoothed velocity is positive as seen in

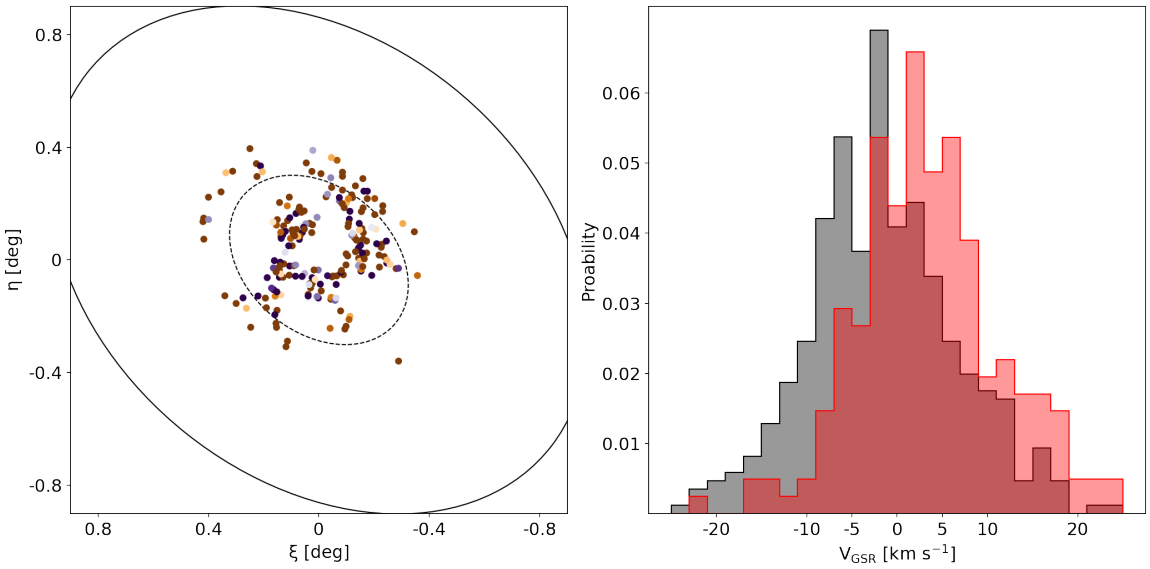

FIGURE 4.3: **Left panel:** Spatial distribution of all stars complying with the selection criteria for the ring-structure. **Right panel:** Distribution of the velocities of the ring sample (red histogram) and the control sample (black histogram).

TABLE 4.2: Mean velocity and velocity dispersion calculated for the ring- and control sample using an error-weighted formula and an MCMC approach.

Parameter	ring sample	control sample
$\bar{v}_{\rm offset}$ [km s^{-1}], formula	3.20 ± 0.05	-0.45 ± -0.03
σ_V [km s^{-1}], formula	8.84	9.01
$\bar{v}_{\rm offset}$ [km s^{-1}], MCMC	$1.58^{0.43}_{-0.44}$	$-1.23^{0.36}_{0.35}$
σ_V [km s^{-1}], MCMC	$8.51^{+0.31}_{-0.30}$	$8.60^{+0.31}_{-0.30}$

Figure 4.1 (210 stars). A control sample is then defined by all the stars that do not comply with these criteria (434 stars).

Figure 4.3 presents the positions of all stars that comply with the selection criteria as well as the velocity distribution of the two samples. The extended spatial coverage of the current sample compared to Cicuéndez and Battaglia (2018) shows stars further away from the centre to potentially be part of the ring. However, this is also partly due to the rough selection criteria employed for the ring stars in the current analysis. Nevertheless, it is still fruitful to inspect these results carefully.

In the current selection the ring no longer resembles a ring the way it did before. Its shape has changed to more of a spiral structure perhaps like a stellar stream wrapping around the centre of Sextans. Moreover, it is not a smoothly distributed structure, it appears clumpy, which is a property that could already be noticed in Figure 4.1. Looking at the velocity distribution of the ring in the right-hand panel of Figure 4.3 shows that the ring sample velocities have a small but significant offset from the control sample. The mean velocity and velocity dispersion were calculated using a simple error-weighted formula. Additionally, the mean velocity and dispersion were estimated using an MCMC approach. The results of both procedures are presented in Table 4.2.

Comparing our new results to the calculations of Cicuéndez and Battaglia (2018) (their Table 2) it is evident that for the ring sample the mean velocity is similar when considering the results from a simple calculation while for the control sample the mean velocity is comparable for the MCMC derived values. Moreover, all the derived velocity dispersions are significantly higher which could be a result of the larger sample sizes employed in the current analysis. Either way, it seems obvious that a ring-like kinematic substructure is present in Sextans, though its exact properties remain difficult to precisely

define.

Chapter 5

Chemical Analysis

Studying the chemical content of galaxies allows one to deduce what processes have shaped its past. The onset of supernovae, mixing processes in the interstellar medium, and the star-formation history, including star burst episodes perhaps due to tidal interactions with a massive host, can be studied from the chemical enrichment in the galaxy. In order to study the chemical content of Sextans all member stars in the FLAMES low resolution spectroscopy catalogue will be used (556 stars with metallicities) complemented by the high resolution spectroscopy sample presented in Section 2.2.

5.1 Metallicities

Metallicity is an important "simple" tracer for the galactic chemical enrichment processes. Large sample sizes covering a large spatial area and a wide range of stellar ages are available to explore the global metal content and how it built up over time.

The left panel of Figure 5.1 presents the metallicity distribution function of Sextans member stars in the FLAMES sample. As already established, the metal content in Sextans is very broad, ranging from [Fe/H] = −3.5 dex to −1 dex, and bimodal (Battaglia et al., 2011). This metallicity distribution is well-modelled by a sum of two Gaussian profiles with best fitting peak positions and metallicity dispersions $[\mathrm{Fe/H}]_{\mathrm{high}} = -1.98 \pm 0.05$ with dispersion $\sigma_{[\mathrm{Fe/H}]} = 0.30 \pm 0.02$ and $[\mathrm{Fe/H}]_{\mathrm{low}} = -2.81 \pm 0.02$ with dispersion $\sigma_{[\mathrm{Fe/H}]} = 0.18 \pm 0.02$, for the high- and low-metallicity contributions respectively. Both of these values are roughly consistent with Battaglia et al. (2011). The current sample contains more stars with low metallicities which comes from the larger spatial extent and the improved sampling at greater distances from the centre of the current catalogue compared to Battaglia et al. (2011).

This point is driven home further in the right panel of Figure 5.1 and the left-hand panel of Figure 5.2 which show the metallicity as a function of elliptical radius and the spatial distribution of the metallicity, respectively. From these plots it becomes very clear that the metal-rich stars mainly reside in the centre of Sextans, while the outskirts are dominated by the more metal-poor stars. Stars with metallicities higher than −2 dex are absent beyond 1° from the centre, while in the central region the full range of metallicities is present.

A clear metallicity gradient is present in Sextans. After binning the data in elliptical annuli increasing in width with radius to keep a statistically significant number of stars in each bin, this gradient is clearly visible in the right-hand panel of Figure 5.1. A simple linear fit through these points gives a central metallicity [Fe/H] = -2.06 ± 0.14 dex and a gradient of -0.37 ± 0.09 dex deg^{-1} = −0.13 dex $\mathrm{R_h^{-1}}$. Comparing this to Carina (−0.0047 dex arcmin^{-1} = −0.04 dex $\mathrm{R_h^{-1}}$, Koch et al. (2006)), Cetus (−0.033 dex arcmin^{-1} = −0.11 dex $\mathrm{R_h^{-1}}$, Taibi et al. (2018)), and Sculptor (−0.024 dex arcmin^{-1} = −0.27 dex $\mathrm{R_h^{-1}}$ Martínez-Vázquez et al. (2016)) it is evident that the metallicity gradient in Sextans is much stronger than in Carina, similar in magnitude to Cetus, but much weaker than the one found in Sculptor given the extent of the system. It must be noted that in Sextans, like

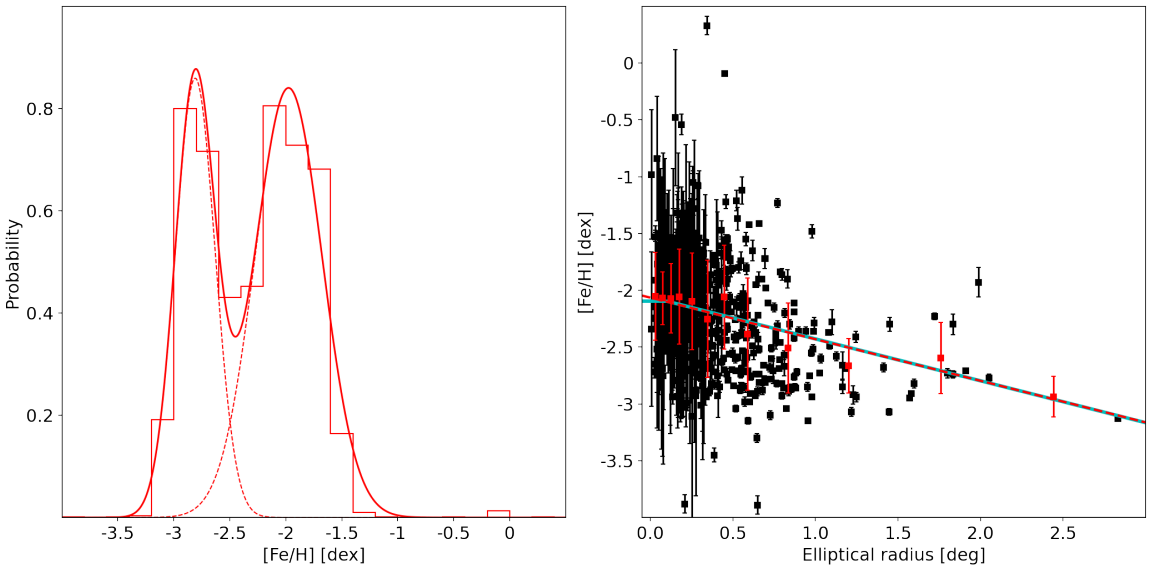

FIGURE 5.1: **Left panel:** Error weighted metallicity distribution function for the Sextans member stars. The thick red line shows the best fitting double Gaussian profile to the histogram, the dashed lines show contributions from the constituting single Gaussians. **Right panel:** Radial distribution of the metallicities. The red datapoints are the mean metallicity in elliptical bins of varying width, the errorbars represent the dispersion in the metallicity. The dashed red line gives the decline of the mean metallicity as a function of elliptical radius. The dashed cyan line also gives a decline but with a plateau in the centre.

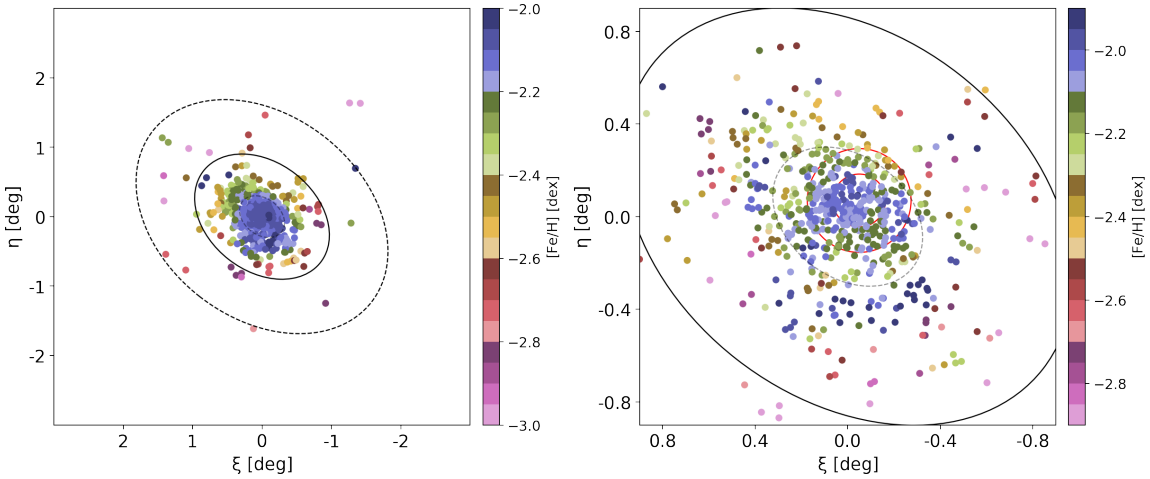

FIGURE 5.2: **Left panel:** Spatial distribution of the metallicities of Sextans member stars, smoothed with a meanfilter with a radius of 0.2°. **Right panel:** Zooming in to the centre of Sextans, smoothed with meanfilter with a radius of 5 arcmin. The red circles indicate the position of the ring-structure described in Section 4.3. The ellipses show the one half-light radius, three half-light radii, and tidal radius.

is the case in Cetus and Sculptor, in the very central region the mean metallicity remains roughly constant and then starts to decline more rapidly beyond 0.5° in the case of Sextans. A model with a central plateau is matched well and gives a slightly lower central metallicity and a very slightly stronger metallicity gradient. However, within standard errors this gradient is no different from the one derived with a more simple linear model. This model is also presented in the right panel of Figure 5.1 with the cyan line (lying below the red line due to their similar strength of the gradient).

Some simulations of dwarf galaxies have found similar behaviour of the stellar metallicities as a function of radius: a central plateau followed by a clear decline (e.g. Schroyen et al., 2013). It is argued that the

presence of a strong metallicity gradient is a direct result of the star-formation history of non-rotating galaxies. While rotating galaxies are also found to have metallicity gradients, it is believed that the angular momentum in these systems sets a centrifugal barrier preventing gas to efficiently funnel to the centre thus producing a shallower metallicity gradient (Leaman et al., 2013). Dwarf spheroidals possess little angular momentum and thus the star formation becomes more centrally concentrated over time, building up and maintaining a metallicity gradient over time. The long survival times of the metallicity gradients in dSphs is attributed to the pressure support in that allows hardly any radial migration of stars over long periods of time. In contrast to massive spiral galaxies where the rotation can cause significant radial migration of interstellar material, and quickly decrease the strength of their metallicity gradients (Magrini et al., 2016; Minchev et al., 2018).

Concerning the ring-structure discussed in Section 4.3 and its presence in the metallicity distribution of Sextans, from the right-hand panel of Figure 5.2 it is clear that it is hard, if not impossible, to pick out the ring structure by eye in the spatial distribution of the metallicities. Even when its position from the radial velocities is indicated with the red circles, it remains very hard to pick out a ring-structure. Contrary to Cicuéndez and Battaglia (2018), who found a different metallicity for the ring based on magnesium triplet equivalent widths, the current more accurate metallicity analysis finds no such signature.

5.2 Chemical Abundances

Detailed abundances of a range of chemical elements are useful to constrain many processes that shape a galaxy. Since the bulk of the high resolution spectroscopic sample is identical to Theler et al. (2020), the analysis in this section will be very comparable.

Figures 5.3 and 5.4 show the abundances of the individual alpha-elements (Mg, Ca, Ti) and the combined alpha elements. In Figure 5.3 a common trend between the alpha-elements is visible: a plateau at constant (supersolar) [X/Fe] followed by a knee and decrease to subsolar values. The knee position is the same for the three elements, but the scatter is different for the different elements. Reichert et al. (2020) reported the possible presence of a double knee in Sextans based only on the magnesium abundance. However, this is likely due to the large scatter, as from the current data it could be present in magnesium, but certainly it is not present in the calcium abundances.

This possible double knee completely disappears when the alpha-elements are combined, as presented in Figure 5.4. The stars in Sextans follow the trend already present in the individual abundances, but with significantly smaller scatter. Apart from the [α/Fe], Figure 5.4 also presents the combination of Magnesium and Calcium as it allows to probe the plateau to lower metallicities although with increased scatter. The trend in the alpha-elements shown by the Sextans stars is compared to Sculptor, also shows this behaviour. A plateau with supersolar [α/Fe] at low metallicities is consistent with initial pollution of the interstellar medium (ISM) only by supernovae type II (SN II), which explode on relatively short time-scales and produce large amounts of alpha-elements. At later times SN Ia start to significantly increase the iron-peak elements in the ISM composition, leading to a decrease in the relative abundance of alpha-elements. In the Milky Way this happens at a relatively high metallicity compared to Sextans and Sculptor, small systems, this knee occurs already at [α/Fe] ~ -2 for Sextans and [α/Fe] ~ -1.8 for Sculptor.

The similar locations of the knee indicates comparable star formation efficiencies in both systems at early times. The slope of the decrease is determined by the relative amounts of ejected materials of SN Ia and SN II. Rapidly quenched systems will show a sharper decline in [α/Fe] compared to systems with more extended star-formation histories. Sextans shows a steeper decline than Sculptor, indicating it was quenched more quickly.

Moving to the Iron-peak elements (Sc, Cr, Mn, Ni, Co, Zn), Figure 5.5 presents the abundances of scandium, nickel, and chromium, respectively. Manganese, cobalt, and zinc are not considered as only very few member stars in the sample have measured abundances. Scandium is mainly produced in SN

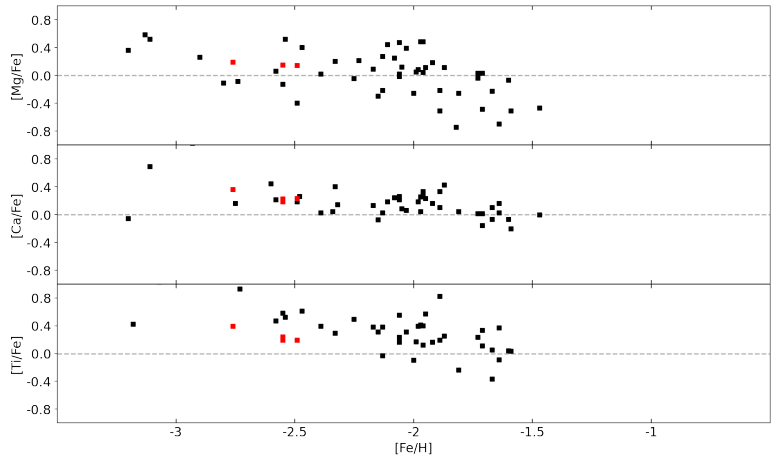

FIGURE 5.3: **From top to bottom:** magnesium, calcium, and titanium abundances as a function of [Fe/H]. In black the literature results (Theler et al., 2020). The red squares present the new UVES data reduced with our pipeline described in Section 3.1.

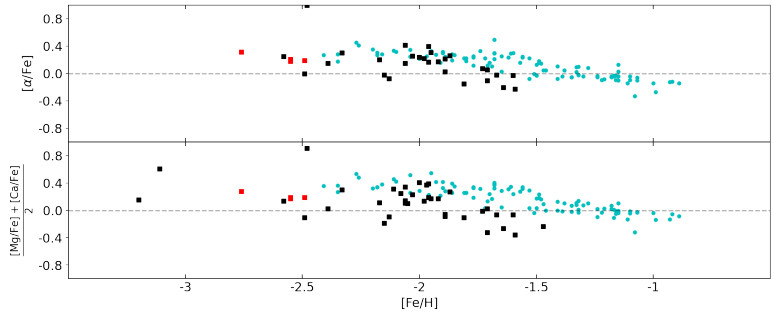

FIGURE 5.4: **Top panel:** Combination of the three alpha-elements in Figure 5.3. **Bottom panel:** Combination of the magnesium and calcium abundances as a function of [Fe/H]. In black are the literature results, red squares are our new UVES results. The cyan points are sculptor data (Hill et al., 2019).

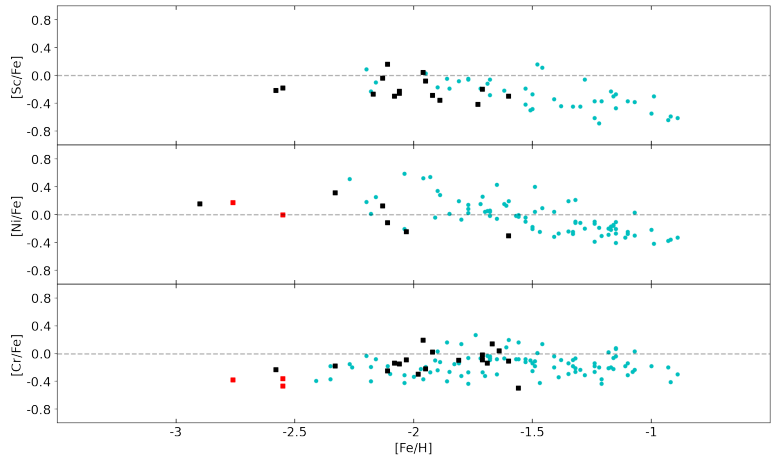

FIGURE 5.5: **From top to bottom:** scandium, nickel, and chromium abundances relative to [Fe/H]. Colour coding is as in Figure 5.4.

II (Battistini and Bensby, 2015) and thus is expected to follow a similar trend as the alpha-elements. From Figure 5.5 it is hard to clearly discern this trend, no plateau is visible due to a lack of stars at low metallicities. However, a decrease in scandium abundance from [Fe/H] ~ -2 (the location of the knee from the alpha-elements) is present, indicating that a common origin is possible. Compared to the Sculptor stars, this knee happens slightly earlier and has a steeper slope than the alpha-elements.

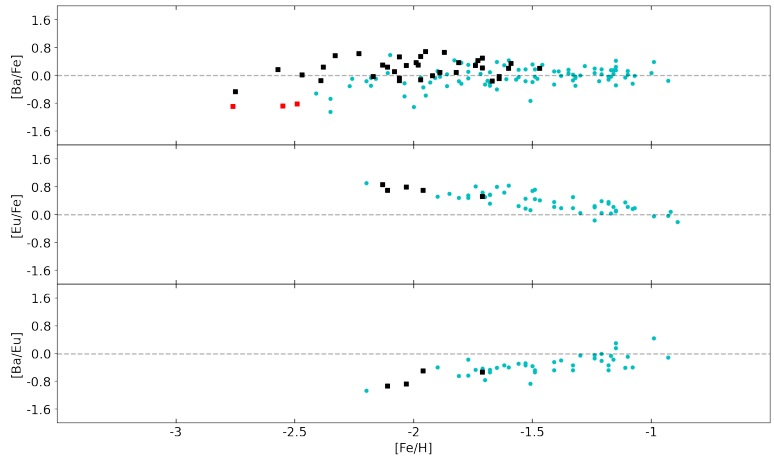

FIGURE 5.6: **From top to bottom:** barium, and europium abundances relative to [Fe/H] and [Ba/Eu] abundance ratio all as a function of [Fe/H]. Colour coding is identical to Figure 5.4.

Moreover, while a plateau is visible for the Sculptor stars, it is not elevated above solar values of [Sc/Fe] which is also the case for the two Sextans stars around [Fe/H] $= -2.5$.

Nickel (and also cobalt) is different from Scandium, as it can also be produced in large quantities in SN Ia (Timmes et al., 2003; Travaglio et al., 2005). From Figure 5.5 a decrease in nickel abundance beyond [Fe/H] ~ -2 is visible in the Sextans data, roughly coinciding with the knee in the alpha-elements. This indicates that the yield nickel in SN Ia is lower than the production of iron. This decline coinciding with the alpha-knee is also present in the Sculptor data. For the Sextans data the location of the knee in the nickel abundances seems to be shifted to lower metallicities relative to the alpha-knee. However, the location of this knee is very uncertain due to the very limited number of datapoints and large uncertainties in the abundances.

The final iron-peak element with a significant number of measurements in Sextans is chromium, which is presented in the lower panel of Figure 5.5. The chromium trend in Sextans is similar to the Sculptor data: the chromium abundance increases with [Fe/H]. Bergemann and Cescutti (2010) showed that this (linear) increase is the effect of neglecting non local thermodynamic equilibrium (NLTE) effects in line formation for metal-poor stars. These NLTE corrections move [Cr/Fe] closer to solar values over the whole metallicity range. The chromium abundance beyond the alpha-knee remains solar, implying similar yields of chromium in both SN Ia and SN II.

The neutron-capture elements barium and europium are used to study the slow- (s) and rapid (r) neutron-capture processes and their relative importance. Barium is predominantly produced by the s-process at higher metallicities and europium by the r-process. At the lowest metallicities, detections of europium are hard. However, a decline in [Eu/Fe] is present at higher metallicities indicating that the r-process cannot keep up with the chemical enrichment of SN Ia. Barium shows a large scatter at low metallicity followed by a plateau slightly above the solar level. Moreover, the scatter in [Ba/Fe] keeps decreasing with increasing [Fe/H]. Both of these trends are in common between Sextans and Sculptor.

The ratio between barium and europium can be used to study the relative contribution of the r- and s-process to their abundances. An increasing trend of [Ba/Eu] is present with increasing [Fe/H] reflecting the drop in [Eu/Fe] while barium forms a plateau. As [Ba/Eu] is sub-solar at low metallicities this indicates that in this regime barium is mainly produced by the r-process, while at higher metallicity the s-process starts to contribute through asymptotic giant branch (AGB) stars. This "high" metallicity regime is not probed by the Sextans sample, but given that Sextans and Sculptor follow similar chemical trends in the neutron-capture elements, a similar fraction of SN Ia and low metallicity AGBs can be expected.

Chapter 6

Chemodynamic Analysis

Now that the kinematic and chemical information each have been explored separately, it is time to combine their powers. The ingredients of a simple chemodynamic analysis will be described in this chapter to disentangle different stellar populations in Sextans.

The procedure of distinguishing stellar populations and ascribing individual stars different populations is rarely straightforward. Many dSphs appear to host more than one stellar population. However, for Sextans this case is even more complicated due to the presence of a ring-structure manifesting itself in velocity- and metallicity space described in Section 4.3 and Cicuéndez and Battaglia (2018).

6.1 A Two-Component Galaxy

To ascribe stars to their respective population, the likelihood for each star is defined using the two component model, one for the metal-rich (MR) population and one for the extended metal-poor (MP) population

$$\mathcal{L} = f_{\mathrm{met}}\mathcal{L}_{\mathrm{MR}} + (1 - f_{\mathrm{met}})\mathcal{L}_{\mathrm{MP}} \tag{6.1}$$

where the MR and MP subscripts refer to the metal-rich and metal-poor population respectively. Both of these likelihood terms are expanded using a spatial component described by a Plummer density in which the half-light radius is left as a free parameter to describe the extent of the populations. The line-of-sight velocity distribution and the metallicity distribution for both components is described using a Gaussian with a mean and dispersion for the velocities and metallicities, respectively.

This brings the total number of free parameters to 11: the normalization factor f_{met}, the half-light radii for both components, two mean velocities and velocity dispersions, and finally two mean metallicities and associated dispersions. These parameters will be sampled making use of the PyMC3 package again (Salvatier et al., 2016). Priors are all chosen to be Gaussian distributions with a truncated variant where applicable, except for the normalization factor which has a uniform prior in between 0 and 1. All parameters of the prior are listed in Table 6.1 (MP+MR model column) as well as the maximum a-posteriori estimates of the sampling process.

From the estimated parameters, it becomes clear that the metal-poor and metal-rich components are significantly different in a few key areas: the half-light radius for the metal-poor population is a lot larger, about 1.5 times that of the metal-rich population, and the velocity dispersion is approximately twice as high for the metal-poor population compared to the metal-rich population. This also shows in the histogram of the velocities of the stars in the different components, presented in Figure 6.1, which is very broad for the extended metal-poor component whilst more peaked for the metal-rich component. When the metallicity distribution in Figure 6.1 is considered, it becomes clear that even though the metal-poor component has a lower mean metallicity, a significant number of stars actually have quite high metallicities, i.e. the tail of the distribution extends a long way into the more metal-rich regime, this comes from the few stars with high metallicities at large distances from the centre. At this point

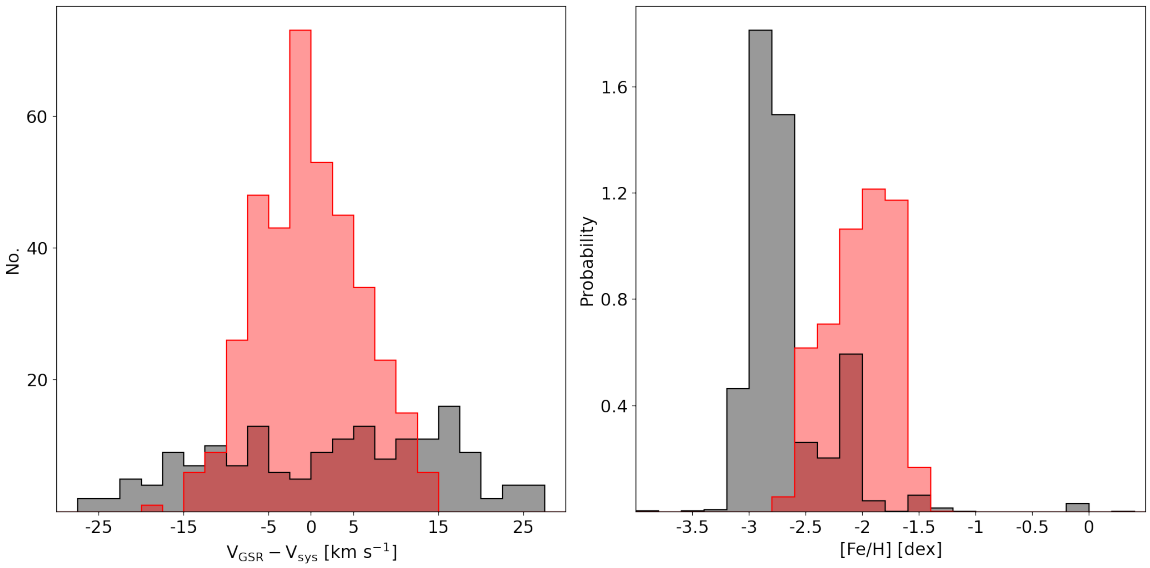

FIGURE 6.1: **Left panel:** Velocity distribution around the systemic velocity for the MP+MR model. **Right panel:** Metallicity distribution function of stars in the MP+MR model. In both cases the red histogram represents the metal-rich component and black the metal-poor component.

the spatial likelihood for the metal-poor component dominates over all other terms in equation 6.1 and the star is placed in the metal-poor component. For this reason the naming of metal-poor and metal-rich is no longer very applicable, calling the two components the hot, diffuse population and the central metal-rich population reflects their properties better.

The presence of multiple stellar populations is common in dSphs. Clearly Sextans is no different in this aspect with the presence of at least two stellar populations: a kinematically hot, spatially extended population and a centrally concentrated metal-rich population. However, it remains challenging to confidently ascribe a star to one population or the other since there is no hard boundary between the populations.

Figure 6.2 presents the line-of-sight velocity and velocity dispersion profile in Sextans for both components. Evidently, these two populations have very different velocity dispersion profiles: the overall dispersion of the central metal-rich component is significantly lower and the profile remains roughly flat out to the last datum, conversely, the hot, diffuse component has a larger dispersion which may decrease with radius, however, the errors also increase with radius so it is also consistent with a flat dispersion profile.

A decreasing velocity dispersion profile in dSphs has been found for the metal-poor component in Fornax (Amorisco and Evans, 2012) and Ursa Minor (Pace et al., 2020), while in Sculptor it is the metal-rich population that shows a declining velocity dispersion (Battaglia et al., 2008) which was also previously the case for Sextans (Battaglia et al., 2011). In all cases the velocity dispersion of the system as a whole remains flat, which is true for Sextans too as was seen in Section 4.2, even though the sub-populations differ from this trend significantly. The difference in characteristics can be the result of the different mechanisms that dominated the formation of the stellar populations.

Several scenarios have been proposed for the formation of distinct stellar populations in dSphs: mergers between small systems, tidal interactions with a massive companion, and supernova feedback. In some hydrodynamical simulations even isolated dwarf galaxies have been shown to be able to host more than one stellar population (Revaz and Jablonka, 2018). Based on simulations Genina et al. (2019) found that most field dwarfs and some satellite systems could form their distinct populations through mergers, which drive already existing metal-poor stars to migrate outwards and heats them dynamically while the remaining gaseous component sinks to the centre, triggering star formation and

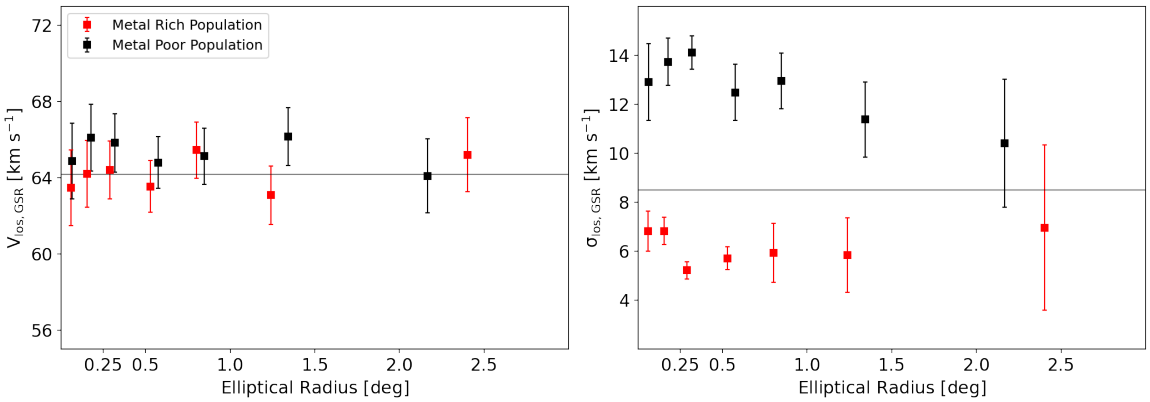

FIGURE 6.2: **Left panel:** Line-of-sight velocity profile for the metal-poor and metal-rich population in Sextans, respectively, in a two-component stellar population model. **Right panel:** Velocity dispersion profile for the same model. Black squares present the data for the hot and diffuse population while red squares are used for the central metal-rich component.

creating the central metal-rich population. Alternatively, in satellites that have retained their gas over extended periods of time, the metal-rich population forms through ram-pressure compression of this gas near pericentre triggering star formation. However, the latter scenario seems unlikely in the case of Sextans as orbital modelling shows that it is currently past its pericentre with an orbital period of 3 Gyr (Casetti-Dinescu et al., 2018; Battaglia et al., 2022) while the star-formation history of Sextans indicates that most of its stars formed over 11 Gyr ago, before it fell into the Milky Way's gravitational potential (Bettinelli et al., 2018).

Moreover, from the analysis of the chemical abundances in Sextans in Section 5.2 it was concluded that star formation in Sextans was quenched relatively quickly. This could have happened after a small merger event as described above when gas falls to the centre quickly triggering the formation of the metal-rich population in which all the remaining gas is consumed leaving the galaxy quiescent afterwards. Even though, based on the current data, this scenario seems most plausible, the case remains complicated for Sextans due to the presence of the ring-structure.

6.2 Analysing the Ring-Structure in Sextans

To study the ring-structure in Sextans, two scenarios are explored: a two-component system in which the main population of Sextans is assumed to be a single stellar population and an explicit component for the ring-structure (SX+ring model). The second option is a three-component model in which the main stellar population of Sextans is split into an extended metal-poor and a central metal-rich component, as was the case in Section 6.1 (MP+MR+Ring model). The likelihood in the two-component model can be written as

$$\mathcal{L} = f_{\rm ring}\mathcal{L}_{\rm ring} + (1 - f_{\rm ring})\mathcal{L}_{\rm SX} \tag{6.2}$$

identical to the previous two-component model, only the labels have changed to reflect the different components. The likelihoods are all split into a spatial, velocity, and metallicity component which functional shapes for Sextans are identical to those in the two-component model. For the ring-structure, the spatial likelihood is described using a Gaussian since it is hard to assume a surface-density profile combined with the ring having a different centre from Sextans. The distance of stars is calculated with respect to a central coordinate (X_c,Y_c) which is relative to the centre of Sextans. The dimensions of the ring are determined using the radius R and the width σ_R. The spatial likelihood for the individual datums in the ring becomes

$$\mathcal{L}_i = \frac{1}{\sqrt{2\pi\sigma_R^2}} \exp\left[-\frac{(x_i - X_c)^2 + (y_i - Y_c)^2 - R^2}{2\sigma_R}\right] \tag{6.3}$$

TABLE 6.1: Maximum a-posteriori estimates of the parameters determining the models described in Sections 6.1 and 6.2.

Parameter	Units	Prior	MP+MR model	SX+Ring model	MP+MR+Ring model
$f_{\rm met}$		[0, 1]	0.59 ± 0.06		0.44 ± 0.08
			Metal-rich		**Metal-rich**
R_h	arcmin	21.4 ± 2.0	16.6 ± 1.0		20.2 ± 1.5
$\bar{V}_{\rm GSR}$	km s^{-1}	64.0 ± 0.3	64.11 ± 0.26		63.00 ± 0.28
σ_V	km s^{-1}	$7.0 \pm .3$	6.09 ± 0.27		5.09 ± 0.29
[Fe/H]	dex	-1.9 ± 0.2	-2.12 ± 0.04		-2.13 ± 0.07
$\sigma_{\rm [Fe/H]}$	dex	0.3 ± 0.1	0.34 ± 0.03		0.47 ± 0.15
			Metal-poor	**Sextans**	**Metal-poor**
R_h	arcmin	21.4 ± 2.0	24.2 ± 1.3	24.2 ± 1.0	24.7 ± 1.3
$\bar{V}_{\rm GSR}$	km s^{-1}	64.0 ± 0.3	64.13 ± 0.29	64.04 ± 0.27	63.25 ± 0.29
σ_V	km s^{-1}	12.0 ± 0.3	12.00 ± 0.29	11.27 ± 0.27	11.92 ± 0.92
[Fe/H]	dex	-2.8 ± 0.2	-2.47 ± 0.06	-2.34 ± 0.04	-2.45 ± 0.05
$\sigma_{\rm [Fe/H]}$	dex	0.3 ± 0.1	0.63 ± 0.04	0.56 ± 0.03	0.53 ± 0.11
				Ring	**Ring**
$f_{\rm ring}$		[0, 1]		0.28 ± 0.04	0.20 ± 0.04
X_c	arcmin	-2.0 ± 1.0		-2.98 ± 0.70	-3.08 ± 0.73
Y_c	arcmin	3.0 ± 1.0		4.19 ± 0.76	4.93 ± 0.85
R	arcmin	10.0 ± 0.5		10.15 ± 0.37	9.68 ± 0.41
σ_R	arcmin	2.0 ± 0.3		3.31 ± 0.23	2.79 ± 0.29
$\bar{V}_{\rm GSR}$	km s^{-1}	64.0 ± 0.3		66.71 ± 0.29	66.96 ± 0.29
σ_V	km s^{-1}	8.0 ± 1.0		6.53 ± 0.54	7.33 ± 0.67
[Fe/H]	dex	-2.1 ± 0.1		-2.04 ± 0.04	-2.04 ± 0.04
$\sigma_{\rm [Fe/H]}$	dex	0.2 ± 0.1		0.21 ± 0.03	0.19 ± 0.04

where x_i and y_i are the individual position of the stars with respect to the centre of Sextans. The velocity and metallicity likelihoods for the ring-structure are described using Gaussian as well, as is the case for the main stellar component of Sextans. In total this model counts 14 parameters: the normalization constant $f_{\rm ring}$, the five parameters describing the population in Sextans, and 8 parameters describing the ring of which 4 are used to describe its shape and location while the other 4 describe the velocity and metallicity distributions.

The three-component model is more complicated, the likelihood in this case can be written as

$$\mathcal{L} = (1 - f_{\rm ring}) f_{\rm met} \mathcal{L}_{\rm MR} + (1 - f_{\rm ring})(1 - f_{\rm met}) \mathcal{L}_{\rm MP} + f_{\rm ring} \mathcal{L}_{\rm ring} \tag{6.4}$$

In this equation the extended metal-poor and central metal-rich component are described identically to the two components in Section 6.1, whilst the ring is described using the ingredients listed above. The three-component model counts a total of 20 parameters that need to be estimated from the data. A total of 10 parameters to describe the stellar population of Sextans, 5 for the metal-poor and 5 for the metal-rich population, 8 that describe the ring, and 2 normalization factors $f_{\rm ring}$ and $f_{\rm met}$.

In both the two- and three-component ring models the parameter spaces are sampled using the PyMC3 package (Salvatier et al., 2016). The results of the sampling procedure are listed in Table 6.1 (column SX+Ring and MP+MR+Ring, respectively). Concerning the parameters describing the ring, the spatial parameters are very comparable between the two models, even though one is much more complicated than the other. However, it must be noted that the three-component model is not well-fit in the sampling, degeneracies between the parameters exist with multimodal posterior distributions in quite a few parameters. This is not the case for the two-component SX+Ring model, which all

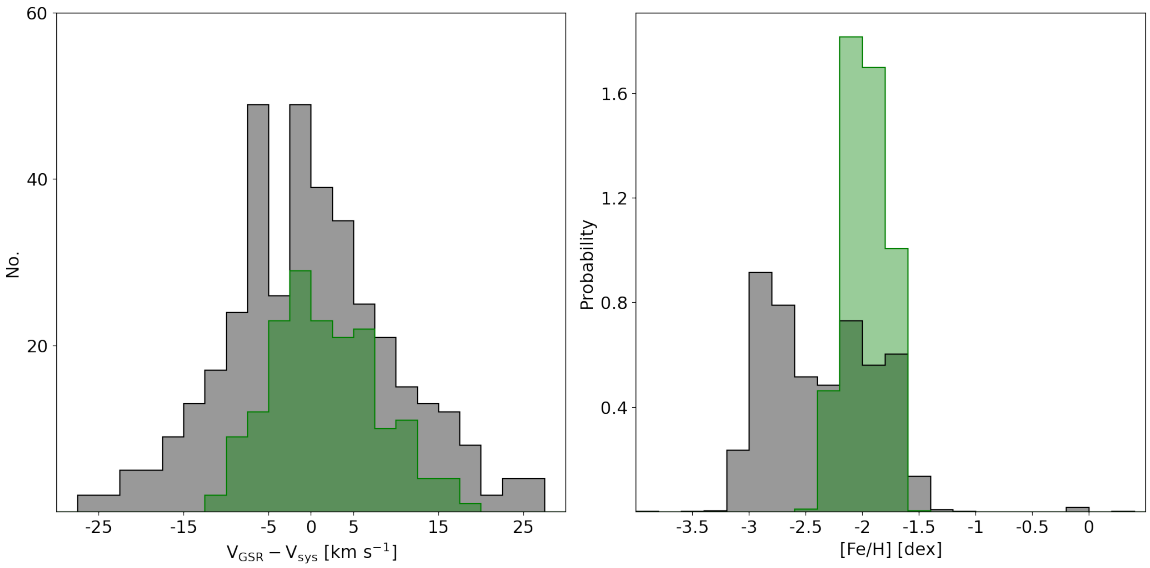

FIGURE 6.3: **Left panel:** Line-of-sight velocity distribution around the systemic velocity of Sextans for the SX+Ring model. **Right panel:** Error weighted metallicity distribution of stars in Sextans for the same model. The black histogram represent the population belonging to Sextans and the green presents the data for the stars belonging to the ring-structure.

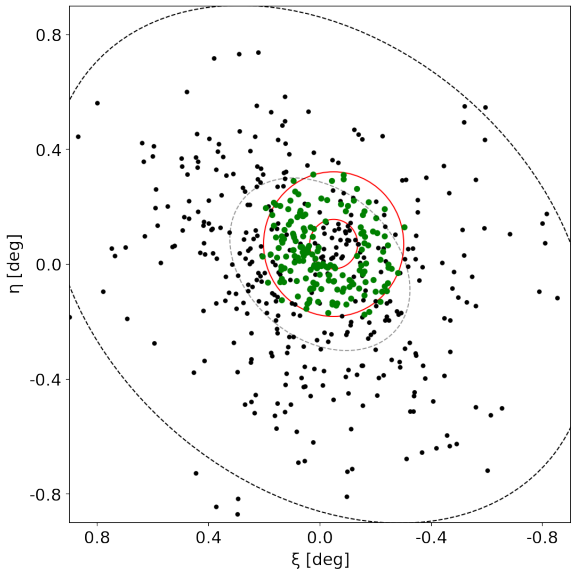

FIGURE 6.4: Spatial distribution of the stars in the ring in the SX+Ring model. Black points represent stars in the Sextans stellar population, while the green points present those that are considered part of the ring. The red circles are in place to guide the eye to the ring.

shows unimodal posterior distributions for all the parameters. From this the applicability of the three-component model is deemed to be limited and it will not be explored further. The main results that will be discussed are those of the two-component SX+Ring model which will also be compared to the MP+MR model described in the previous section.

From the parameter estimation, the values that were determined to best fit the main population of Sextans are very similar to those of the hot, extended model in the MP+MR model. The only significant difference is in the mean metallicity, which is higher in the SX+Ring model. This can be expected since the metal-rich population in Sextans is not explicitly modelled in this case. Concerning the ring: its velocity is offset from the rest of Sextans by about 2.7 km s^{-1}, similar to previous findings (Cicuéndez and Battaglia, 2018). The mean metallicity is significantly higher than the rest of the

population in Sextans. What sparks interest though is the breadth of the metallicity distribution of the ring stars, also combining the result from the parameter estimation with the appearance in the metallicity distribution: based on metallicity dispersion alone it seems hard to believe that the ring is the remnant of an accreted globular cluster.

Figure 6.3 presents the velocity- and metallicity distribution for the two populations of the SX+Ring model, respectively. Based on the metallicity distribution, it is very evident that the ring has a significantly higher mean metallicity. However, the metallicities of stars appearing in the ring also appear in stars that are part of the Sextans population. Moreover, the ring-structure roughly takes the place of the metal-rich population from the MP+MR model in metallicity space and could very well be responsible for the bulk of the metal-rich stars in Sextans. Though due to its limited spatial extent, presented in Figure 6.4, metal-rich stars also remain in the main body of Sextans. Another noticeable thing about the ring is its clumpiness: in some areas the stellar density is much higher (Southeast) that in other areas (North). However, this may also be a result of the sampling of the spectroscopic dataset, which is not uniform even in the central regions.

From the current analysis it is evident that a ring-structure exists in Sextans, though its exact properties remain difficult to constrain. Clearly it has a mean velocity that is offset from Sextans, but in metallicity space it is hard to quantify how different it is. Moreover, due to the limited modelling possibilities, no stars further away from the centre are found that might be associated with the ring. These stars could prove to be crucial in understanding the dynamical nature of the ring and point to a possible mechanism that is responsible for its existence.

6.3 Interpreting the Ring-Structure

The presence of substructure in Sextans has been an ongoing discussion in literature, and earlier studies clearly missed a full picture. Kleyna et al. (2004) reported a kinematically cold substructure in the very centre of Sextans which was also identified photometrically to be redder which could mean that is is more metal rich than its surroundings. Battaglia et al. (2011) found no evidence for this, when the velocity dispersion profiles were calculated the central velocity dispersion was lowest for the metal-poor component which is expected to show up more blue in photometry. The current dataset also finds no support for a cold, metal-rich cluster in the centre of Sextans.

Walker et al. (2006) reported a kinematically cold clump near the core-radius of Sextans, while Kim et al. (2019) detected an overdensity of relatively metal-poor stars about 7 arcmin from the centre based on detailed photometric analysis. Given the data of Cicuéndez and Battaglia (2018) and the current analysis, it seems that Walker et al. (2006) detected a small part of the ring while Kim et al. (2019) saw its centre, which is still part of the Sextans stellar population.

A ring-like structure was found in Andromeda II (Amorisco et al., 2014). However, the ring in And II shows a rather smooth nearly sinusoidal variation of the line-of-sight velocity along the ring, making the authors to interpret it as a low-mass object being accreted. This is not the case in Sextans: the ring-structure shows erratic variations in the line-of-sight velocity, even when stars are binned together based on their position angle along the ring to smooth the signal, making it difficult to reconcile the ring with the infall of a low-mass object.

Detailed chemical abundances could provide more insight into the nature of the ring and its origin. Reichert et al. (2020) reported the possibility of a double knee in the magnesium abundances in Sextans, this was also noted in Section 5.2, which could be caused by the ring-structure in Sextans if it has a different origin than the bulk of the stellar population. Figures 6.5 and 6.6 present the abundances of the individual alpha-elements and the combination of the alpha-elements, respectively, for the ring compared to the main body of Sextans.

Immediately Figures 6.5 and 6.6 show that chemically the ring-structure is indistinguishable from the rest of Sextans: it completely blends into the trend of main Sextans population. This remains true for

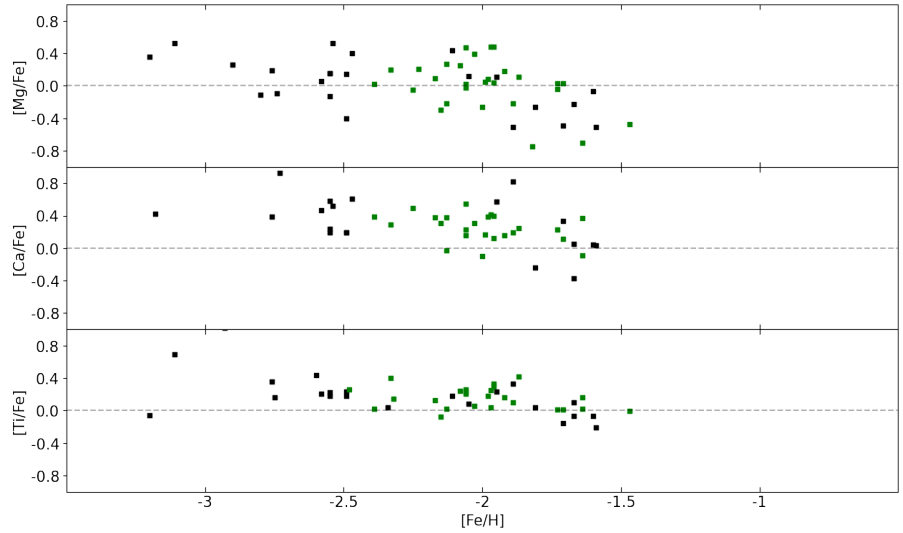

FIGURE 6.5: **From top to bottom:** the abundances of magnesium, titanium, and calcium. In all panels the colour coding is black for stars in the main stellar population of Sextans and green for stars belonging to the ring.

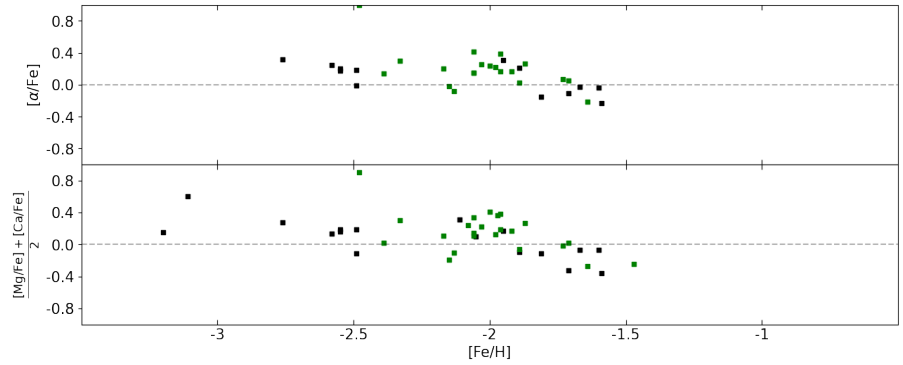

FIGURE 6.6: **Top panel:** alpha element abundances for the stars in Sextans. **Bottom panel:** Combination of the magnesium and calcium abundance to trace the alpha elements to lower metallicities as titanium abundances are not well determined for the lowest metallicities. Colour coding is as in Figure 6.5.

the iron-peak and neutron-capture elements as well, even though these elements have a significantly smaller number of stars in each component. Moreover, the ring-structure is not responsible for the double knee in the magnesium abundances. It seems that the double knee is a result of the large scatter in the magnesium abundances, since it completely disappears when the alpha-elements are combined (Figure 6.6). The fact that the ring-structure is not chemically very different from the main stellar population in Sextans makes it hard to believe that it was accreted, except if the accreted system has had the same chemical evolution as Sextans up to the point that it fell in. It seems more plausible that the stars in the ring formed in-situ and obtained their peculiar kinematics from an interaction event.

One possible interpretation for the ring-structure is to see it as an expanding shell. However, the mechanism causing the expansion is hard, if not impossible, to determine. In order to say anything about the expansion, the mean radial velocity with respect to the centre of the ring is calculated. Which is done by converting the proper motions in R.A. and Dec to polar velocities with respect to the centre of the ring and calculating their mean value. This reveals that the ring is not expanding, but instead is more likely to be contracting at -0.03 ± 0.56 mas yr^{-1}. Given that the ring is approximately 10 arcmin in radius this means that it will have collapsed into the centre within 20 Myr. However, the uncertainties on the individual proper motions are too large to draw any conclusions from this result

about the movement of the ring.

Another possibility that could cause a ring-structure in Sextans without leaving an imprint on the chemical composition of the stellar population is an object passing through, like a dark halo. Starkenburg and Helmi (2015) and Starkenburg et al. (2016a,b) performed zoom-in detailed hydrodynamical simulations of dwarf galaxies interacting with dark matter-only haloes. Even though these simulations focused on dIrrs, rather than dSphs, they showed that dark haloes can leave significant imprints on the stellar population and the overall kinematics of a dwarf galaxy. In particular, Starkenburg and Helmi, 2015 showed that an initially disky dwarf irregular can be transformed into a dwarf spheroidal through such an interaction. Furthermore, Starkenburg et al. (2016a) showed that such a dwarf spheroidal hosts two stellar populations: an extended, old, metal-poor component which was present before the interaction, and a centrally concentrated, metal-rich component directly caused by the interaction event. Whilst this does not explain the formation of the ring, it does present an alternative scenario of dSph formation with two stellar components from dIrrs. Moreover, the possibility that the ring in Sextans was created in a similar interaction is not ruled out. One issue with this scenario is the fact that dark matter-only haloes remain speculative in this context.

A final option to consider for the formation of the ring is the presence of Sextans' nearest neighbour: a globular cluster, Pal 3, residing just outside the tidal radius of Sextans. It is possible that the ring is made up of stars that were tidally stripped from the outskirts of Pal 3. However, the spread in the metallicity distribution of the ring is not consistent with this. Moreover, even though Sextans and Pal 3 appear to be close to each other on the sky they are at different heliocentric distances with Sextans being at 85 kpc (Cicuéndez et al., 2018) and Pal 3 at 92.5 kpc (Baumgardt et al., 2019) and have very different radial velocities. Thus, it is difficult to believe that Sextans and Pal 3 have had an interaction in the past, since they are currently moving towards each other based on their proper motions (Baumgardt et al., 2019). A previous interaction is plausible only if the two are gravitationally connected, which is unlikely as well (Boldrini and Bovy, 2021).

Chapter 7

Conclusion

In this thesis the Sextans dSph galaxy has been investigated in detail through the combination of astrometry, photometry, and low- and high resolution spectroscopy. This extensive dataset has been demonstrated to contain a wealth of information about the stellar populations in Sextans. A novel method to disentangle members from contamination is applied in Section 3 which showed the power of GAIA proper motions in combination with radial velocities to obtain robust and reliable membership probabilities for stars even in the diffuse outskirts of the Sextans dSph.

In Chapters 4 and 5 the two main parts of the dataset were considered separately: line-of-sight velocities and metallicities. This revealed a gradient in the velocities, consistent with rotation of the system around the minor axis. Moreover, a ring-structure first reported by Cicuéndez and Battaglia (2018) was confirmed in the radial velocities of Sextans, though no firm conclusions could be drawn about its origins, partly due to the lack of confidence in selecting stars to be member of the ring.

Chapter 5 described the metallicities and the high resolution chemical abundances of Sextans. A bimodal metallicity distribution was confirmed, along with a clear radial metallicity gradient. Interestingly, no stars with metallicities above -2 dex are found at large distances from the centre of Sextans. Detailed abundances show that the early star formation in Sextans is very similar to the Sculptor dSph, though at later times the two begin to differ. Sextans showing evidence that its star formation was quenched more quickly than Sculptor.

Finally Chapter 6 made full use of the information in the current dataset by combining the kinematics with the metallicity to attempt to disentangle multiple chemodynamic populations. This was done in two different ways to better understand the origin of the bimodal metallicity distribution and its possible connection to the kinematics of the system and investigate the ring-structure in depth. In the first model Sextans was divided in a metal-poor and metal-rich population. This showed that the metal-poor population actually encompasses a long tail extending into the metal-rich regime, its main difference from the metal-rich population being its large spatial extent and high velocity dispersion.

The second model divides the galaxy into a main stellar population and a ring-structure with a distinct radial velocity. This analysis showed the significantly different velocity of the stars in the ring, which was noticed before, combined with a small velocity dispersion. The ring was found to be more metal rich than the main stellar population of Sextans, though this is judged from the mean metallicity since the main population of Sextans does extend into this high metallicity regime. Detailed analysis of the chemical abundances of the alpha-elements, iron-peak elements and neutron-capture elements in the ring showed that it is not distinguishable from the rest of the galaxy. This makes a scenario in which the stars in the ring were deposited by a different progenitor, like a globular cluster, unlikely. A globular cluster progenitor was already deemed unlikely based on the metallicity dispersion of the ring. The current analysis shows that the ring-structure is clearly present, even in a dataset different from Cicuéndez and Battaglia (2018). However, its origin remains unclear. Possible scenarios have been discussed, but the current data do not favour one scenario over another.

Future research combining chemical and kinematic information should ideally focus on sampling the galaxy more uniformly with better coverage in the outskirts of Sextans. In Section 3.2 it was shown that the GAIA catalogue contains over 1500 highly likely members of Sextans, depending on where you place the membership criterion this can go up to roughly 2300 member stars. With upcoming instruments like WEAVE and 4MOST, these numbers of stars should become easily observable. Large homogeneous datasets should be able to confirm the distinct chemodynamic stellar populations with more certainty and possibly constrain the nature of the ring in Sextans.

Bibliography

Alfaro-Cuello, M. et al. (Mar. 2020). "A Deep View into the Nucleus of the Sagittarius Dwarf Spheroidal Galaxy with MUSE. II. Kinematic Characterization of the Stellar Populations". In: *The Astrophysical Journal* 892.1, 20, p. 20. DOI: 10.3847/1538-4357/ab77bb.

Amorisco, N. C. and N. W. Evans (Sept. 2012). "A Troublesome Past: Chemodynamics of the Fornax Dwarf Spheroidal". In: *The Astrophysical Journal Letters* 756.1, L2, p. L2. DOI: 10.1088/2041-8205/756/1/L2.

Amorisco, N. C., N. W. Evans, and G. van de Ven (Mar. 2014). "The remnant of a merger between two dwarf galaxies in Andromeda II". In: *Nature* 507.7492, pp. 335–337. DOI: 10.1038/nature12995.

Aoki, M., W. Aoki, and P. François (Apr. 2020). "Chemical abundance analysis of extremely metal-poor stars in the Sextans dwarf spheroidal galaxy". In: *Astronomy and Astrophysics* 636, A111, A111. DOI: 10.1051/0004-6361/201936535.

Asplund, M. et al. (Sept. 2009). "The Chemical Composition of the Sun". In: *Annual Reviews of Astronomy and Astrophysics* 47.1, pp. 481–522. DOI: 10.1146/annurev.astro.46.060407.145222.

Battaglia, G. et al. (Nov. 2006). "The DART imaging and CaT survey of the Fornax dwarf spheroidal galaxy". In: *Astronomy and Astrophysics* 459.2, pp. 423–440. DOI: 10.1051/0004-6361:20065720.

Battaglia, G. et al. (July 2008). "The Kinematic Status and Mass Content of the Sculptor Dwarf Spheroidal Galaxy". In: *The Astrophysical Journal Letters* 681.1, p. L13. DOI: 10.1086/590179.

Battaglia, G. et al. (Mar. 2009). "The mass content of the Sculptor dwarf spheroidal galaxy". In: *The Galaxy Disk in Cosmological Context*. Ed. by J. Andersen et al. Vol. 254, pp. 61–66. DOI: 10.1017/S1743921308027397.

Battaglia, G. et al. (Feb. 2011). "Study of the Sextans dwarf spheroidal galaxy from the DART Ca II triplet survey". In: *Montly Notices of the Royal Astronomical Society* 411.2, pp. 1013–1034. DOI: 10.1111/j.1365-2966.2010.17745.x.

Battaglia, G. et al. (Jan. 2022). "Gaia early DR3 systemic motions of Local Group dwarf galaxies and orbital properties with a massive Large Magellanic Cloud". In: *Atronomy and Astrophysics* 657, A54, A54. DOI: 10.1051/0004-6361/202141528.

Battaglia, G. and C. Nipoti (May 2022). "Stellar dynamics and dark matter in Local Group dwarf galaxies". In: *Nature Astronomy, Advanced Online Publication*. DOI: 10.1038/s41550-022-01638-7.

Battistini, C. and T. Bensby (May 2015). "The origin and evolution of the odd-Z iron-peak elements Sc, V, Mn, and Co in the Milky Way stellar disk". In: *Astronomy and Astrophysics* 577, A9, A9. DOI: 10.1051/0004-6361/201425327.

Baumgardt, H. et al. (Feb. 2019). "Mean proper motions, space orbits, and velocity dispersion profiles of Galactic globular clusters derived from Gaia DR2 data". In: *Monthly Notices of the Royal Astronomical Society* 482.4, pp. 5138–5155. DOI: 10.1093/mnras/sty2997.

Bergemann, M. and G. Cescutti (Nov. 2010). "Chromium: NLTE abundances in metal-poor stars and nucleosynthesis in the Galaxy". In: *Astronomy and Astrophysics* 522, A9, A9. DOI: 10.1051/0004-6361/201014250.

Bettinelli, M. et al. (May 2018). "The star formation history of the Sextans dwarf spheroidal galaxy: a true fossil of the pre-reionization era". In: *Monthly Notices of the Royal Astronomical Society* 476.1, pp. 71–79. DOI: 10.1093/mnras/sty226.

Bettinelli, M. et al. (Aug. 2019). "The star formation history of the Sculptor dwarf spheroidal galaxy". In: *Monthly Notices of the Royal Astronomical Society* 487.4, pp. 5862–5873. DOI: 10.1093/mnras/stz1679.

Bianchini, P., R. Ibata, and B. Famaey (Dec. 2019). "Exploring the Outskirts of Globular Clusters: The Peculiar Kinematics of NGC 3201". In: *The Astrophysical Journal Letters* 887.1, L12, p. L12. DOI: 10.3847/2041-8213/ab58d1.

Blanco-Cuaresma, S. et al. (Sept. 2014). "Determining stellar atmospheric parameters and chemical abundances of FGK stars with iSpec". In: *Astronomy and Astrophysics* 569, A111, A111. DOI: 10.1051/0004-6361/201423945.

Blanco-Cuaresma, S. (June 2019). "Modern stellar spectroscopy caveats". In: *Monthly Notices of the Royal Astronomical Society* 486.2, pp. 2075–2101. DOI: 10.1093/mnras/stz549.

Boldrini, P. and J. Bovy (June 2021). "No globular cluster progenitors in Milky Way satellite galaxies". In: *arXiv e-prints*, arXiv:2106.09419, arXiv:2106.09419.

Bradford, J. D. et al. (Dec. 2011). "Structure and Dynamics of the Globular Cluster Palomar 13". In: *The Astrophysical Journal* 743.2, 167, p. 167. DOI: 10.1088/0004-637X/743/2/167.

Buonanno, R. et al. (July 1998). "The Ages of the Globular Clusters in the Fornax Dwarf Galaxy". In: *The Astrophysical Journal Letters* 501.1, pp. L33–L36. DOI: 10.1086/311436.

Carlberg, R. G. and C. J. Grillmair (Dec. 2021). "Testing for Dark Matter in the Outskirts of Globular Clusters". In: *The Astrophysical Journal* 922.2, 104, p. 104. DOI: 10.3847/1538-4357/ac289f.

Carretta, E. and R. G. Gratton (Jan. 1997). "Abundances for globular cluster giants. I. Homogeneous metallicities for 24 clusters". In: *Astronomy and Astrophysics Supplement Series* 121, pp. 95–112. DOI: 10.1051/aas:1997116.

Casetti-Dinescu, D. I., T. M. Girard, and M. Schriefer (Jan. 2018). "Proper motion of the Sextans dwarf galaxy from Subaru Suprime-Cam data". In: *Monthly Notices of the Royal Astronomical Society* 473.3, pp. 4064–4076. DOI: 10.1093/mnras/stx2645.

Cicuéndez, L. and G. Battaglia (Oct. 2018). "Appearances can be deceiving: clear signs of accretion in the seemingly ordinary Sextans dSph". In: *Monthly Notices of the Royal Astronomical Society* 480.1, pp. 251–260. DOI: 10.1093/mnras/sty1748.

Cicuéndez, L. et al. (Jan. 2018). "Tracing the stellar component of low surface brightness Milky Way dwarf galaxies to their outskirts. I. Sextans". In: *Astronomy and Astrophysics* 609, A53, A53. DOI: 10.1051/0004-6361/201731450.

Dalton, G. et al. (July 2018). "Construction progress of WEAVE: the next generation wide-field spectroscopy facility for the William Herschel Telescope". In: *Ground-based and Airborne Instrumentation for Astronomy VII*. Ed. by C. J. Evans, L. Simard, and H. Takami. Vol. 10702. Society of Photo-Optical Instrumentation Engineers (SPIE) Conference Series, 107021B, 107021B. DOI: 10.1117/12.2312031.

de Jong, R. S. et al. (Mar. 2019). "4MOST: Project overview and information for the First Call for Proposals". In: *The Messenger* 175, pp. 3–11. DOI: 10.18727/0722-6691/5117.

Dekel, A. and J. Silk (Apr. 1986). "The Origin of Dwarf Galaxies, Cold Dark Matter, and Biased Galaxy Formation". In: *The Astrophysical Journal* 303, p. 39. DOI: 10.1086/164050.

Dressler, A. (Mar. 1980). "Galaxy morphology in rich clusters: implications for the formation and evolution of galaxies." In: *The Astrophysical Journal* 236, pp. 351–365. DOI: 10.1086/157753.

Efstathiou, G. (May 1992). "Suppressing the formation of dwarf galaxies via photoionization". In: *Monthly Notices of the Royal Astronomical Society* 256.2, 43P–47P. DOI: 10.1093/mnras/256.1.43P.

Evans, D. W. et al. (Aug. 2018). "Gaia Data Release 2. Photometric content and validation". In: *Astronomy and Astrophysics* 616, A4. DOI: 10.1051/0004-6361/201832756.

Freudling, W. et al. (Nov. 2013). "Automated data reduction workflows for astronomy. The ESO Reflex environment". In: *Astronomy and Astrophysics* 559, A96, A96. DOI: 10.1051/0004-6361/201322494.

Gaia Collaboration et al. (May 2021). "Gaia Early Data Release 3. Summary of the contents and survey properties". In: *Astronomy and Astrophysics* 649, A1, A1. DOI: 10.1051/0004-6361/202039657.

Genina, A. et al. (Sept. 2019). "The distinct stellar metallicity populations of simulated Local Group dwarfs". In: *Monthly Notices of the Royal Astronomical Society* 488.2, pp. 2312–2331. DOI: 10.1093/mnras/stz1852.

Grebel, E. K. and I. Gallagher John S. (Aug. 2004). "The Impact of Reionization on the Stellar Populations of Nearby Dwarf Galaxies". In: *The Astrophysical Journal Letters* 610.2, pp. L89–L92. DOI: 10.1086/423339.

Gustafsson, B. et al. (Aug. 2008). "A grid of MARCS model atmospheres for late-type stars. I. Methods and general properties". In: *Astronomy and Astrophysics* 486.3, pp. 951–970. DOI: 10.1051/0004-6361:200809724.

Hermosa Muñoz, L. et al. (Feb. 2020). "Kinematic and metallicity properties of the Aquarius dwarf galaxy from FORS2 MXU spectroscopy". In: *Astronomy and Astrophysics* 634, A10, A10. DOI: 10.1051/0004-6361/201936136.

Hill, V. et al. (June 2019). "VLT/FLAMES high-resolution chemical abundances in Sculptor: a textbook dwarf spheroidal galaxy". In: *Astronomy and Astrophysics* 626, A15, A15. DOI: 10.1051/0004-6361/201833950.

Ibata, R. et al. (Feb. 2013). "Do globular clusters possess dark matter haloes? A case study in NGC 2419". In: *Monthly Notices of the Royal Astronomical Society* 428.4, pp. 3648–3659. DOI: 10.1093/mnras/sts302.

Ibata, R. A., G. Gilmore, and M. J. Irwin (July 1994). "A dwarf satellite galaxy in Sagittarius". In: *Nature* 370.6486, pp. 194–196. DOI: 10.1038/370194a0.

Irwin, M. and D. Hatzidimitriou (Dec. 1995). "Structural parameters for the Galactic dwarf spheroidals". In: *Monthly Notices of the Royal Astronomical Society* 277.4, pp. 1354–1378. DOI: 10.1093/mnras/277.4.1354.

Irwin, M. J. et al. (May 1990). "A new satellite galaxy of the Milky Way in the constellation of Sextans." In: *Monthly Notices of the Royal Astronomical Society* 244, 16P–19.

Kauffmann, G., S. D. M. White, and B. Guiderdoni (Sept. 1993). "The formation and evolution of galaxies within merging dark matter haloes." In: *Monthly Notices of the Royal Astronomical Society* 264, pp. 201–218. DOI: 10.1093/mnras/264.1.201.

Kim, H.-S. et al. (Jan. 2019). "A Possible Relic Star Cluster in the Sextans Dwarf Galaxy". In: *The Astrophysical Journal Letters* 870.1, L8, p. L8. DOI: 10.3847/2041-8213/aaf885.

Kleyna, J. T. et al. (June 1998). "A V and I CCD Mosaic Survey of the Ursa Minor Dwarf Spheroidal Galaxy". In: *The Astronomical Journal* 115.6, pp. 2359–2368. DOI: 10.1086/300360.

Kleyna, J. T. et al. (Nov. 2004). "A photometrically and kinematically distinct core in the Sextans dwarf spheroidal galaxy". In: *Monthly Notices of the Royal Astronomical Society* 354.4, pp. L66–L72. DOI: 10.1111/j.1365-2966.2004.08434.x.

Koch, A. et al. (Feb. 2006). "Complexity on Small Scales: The Metallicity Distribution of the Carina Dwarf Spheroidal Galaxy". In: *The Astronomical Journal* 131.2, pp. 895–911. DOI: 10.1086/499490.

Kormendy, J. et al. (May 2009). "Structure and Formation of Elliptical and Spheroidal Galaxies". In: *The Astrophysical Journal Supplement* 182.1, pp. 216–309. DOI: 10.1088/0067-0049/182/1/216.

Kravtsov, A. V., O. Y. Gnedin, and A. A. Klypin (July 2004). "The Tumultuous Lives of Galactic Dwarfs and the Missing Satellites Problem". In: *The Astrophysical Journal* 609.2, pp. 482–497. DOI: 10.1086/421322.

Larsen, S. S., J. P. Brodie, and J. Strader (Oct. 2012). "Detailed abundance analysis from integrated high-dispersion spectroscopy: globular clusters in the Fornax dwarf spheroidal". In: *Astronomy and Astrophysics* 546, A53, A53. DOI: 10.1051/0004-6361/201219895.

Law, D. R. and S. R. Majewski (Aug. 2010). "Assessing the Milky Way Satellites Associated with the Sagittarius Dwarf Spheroidal Galaxy". In: *The Astrophysical Journal* 718.2, pp. 1128–1150. DOI: 10.1088/0004-637X/718/2/1128.

Leaman, R. et al. (Apr. 2013). "The Comparative Chemical Evolution of an Isolated Dwarf Galaxy: A VLT and Keck Spectroscopic Survey of WLM". In: *The Astrophysical Journal* 767.2, 131, p. 131. DOI: 10.1088/0004-637X/767/2/131.

Lee, M. G. et al. (Sept. 2009). "Star Formation History and Chemical Evolution of the Sextans Dwarf Spheroidal Galaxy". In: *The Astrophysical Journal* 703.1, pp. 692–701. DOI: 10.1088/0004-637X/703/1/692.

Lora, V. et al. (June 2019). "Cold, Old, and Metal-poor: New Stellar Substructures in the Milky Way's Dwarf Spheroidals". In: *The Astrophysical Journal* 878.2, 152, p. 152. DOI: 10.3847/1538-4357/ab1b71.

Lucchesi, R. et al. (Dec. 2020). "Homogeneity in the early chemical evolution of the Sextans dwarf spheroidal galaxy". In: *Astronomy and Astrophysics* 644, A75, A75. DOI: 10.1051/0004-6361/202037534.

Magrini, L. et al. (Apr. 2016). "Metallicity gradients in local Universe galaxies: Time evolution and effects of radial migration". In: *Astronomy and Astrophysics* 588, A91, A91. DOI: 10.1051/0004-6361/201527799.

Marigo, P. et al. (May 2008). "Evolution of asymptotic giant branch stars. II. Optical to far-infrared isochrones with improved TP-AGB models". In: *Astronomy and Astrophysics* 482.3, pp. 883–905. DOI: 10.1051/0004-6361:20078467.

Martínez-Vázquez, C. E. et al. (Sept. 2016). "Probing the early chemical evolution of the Sculptor dSph with purely old stellar tracers". In: *Monthly Notices of the Royal Astronomical Society* 461.1, pp. L41–L45. DOI: 10.1093/mnrasl/slw093.

Mashonkina, L. et al. (Aug. 2017a). "The formation of the Milky Way halo and its dwarf satellites; a NLTE-1D abundance analysis. I. Homogeneous set of atmospheric parameters". In: *Astronomy and Astrophysics* 604, A129, A129. DOI: 10.1051/0004-6361/201730779.

Mashonkina, L. et al. (Dec. 2017b). "The formation of the Milky Way halo and its dwarf satellites; a NLTE-1D abundance analysis. II. Early chemical enrichment". In: *Astronomy and Astrophysics* 608, A89, A89. DOI: 10.1051/0004-6361/201731582.

Mashonkina, L. et al. (Jan. 2022). "The formation of the Milky Way halo and its dwarf satellites: A NLTE-1D abundance analysis. V. The Sextans galaxy". In: *Monthly Notices of the Royal Astronomical Society* 509.3, pp. 3626–3642. DOI: 10.1093/mnras/stab3189.

Mayer, L. et al. (Feb. 2001). "Tidal Stirring and the Origin of Dwarf Spheroidals in the Local Group". In: *The Astrophysical Journal Letters* 547.2, pp. L123–L127. DOI: 10.1086/318898.

McConnachie, A. W. (July 2012). "The Observed Properties of Dwarf Galaxies in and around the Local Group". In: *The Astronomical Journal* 144.1, 4, p. 4. DOI: 10.1088/0004-6256/144/1/4.

McConnachie, A. W. and K. A. Venn (Sept. 2020a). "Revised and New Proper Motions for Confirmed and Candidate Milky Way Dwarf Galaxies". In: *The Astronomical Journal* 160.3, 124, p. 124. DOI: 10.3847/1538-3881/aba4ab.

— (Dec. 2020b). "Updated Proper Motions for Local Group Dwarf Galaxies Using Gaia Early Data Release 3". In: *Research Notes of the American Astronomical Society* 4.12, 229, p. 229. DOI: 10.3847/2515-5172/abd18b.

Minchev, I. et al. (Dec. 2018). "Estimating stellar birth radii and the time evolution of Milky Way's ISM metallicity gradient". In: *Monthly Notices of the Royal Astronomical Society* 481.2, pp. 1645–1657. DOI: 10.1093/mnras/sty2033.

Muñoz, R. R., S. R. Majewski, and K. V. Johnston (May 2008). "Modeling the Structure and Dynamics of Dwarf Spheroidal Galaxies with Dark Matter and Tides". In: *The Astrophysical Journal* 679.1, pp. 346–372. DOI: 10.1086/587125.

Pace, A. B. and T. S. Li (Apr. 2019). "Proper Motions of Milky Way Ultra-faint Satellites with Gaia DR2 × DES DR1". In: *The Astrophysical Journal* 875.1, 77, p. 77. DOI: 10.3847/1538-4357/ab0aee.

Pace, A. B. et al. (Aug. 2014). "Evidence for substructure in Ursa Minor dwarf spheroidal galaxy using a Bayesian object detection method". In: *Monthly Notices of the Royal Astronomical Society* 442.2, pp. 1718–1730. DOI: 10.1093/mnras/stu938.

Pace, A. B. et al. (July 2020). "Multiple chemodynamic stellar populations of the Ursa Minor dwarf spheroidal galaxy". In: *Monthly Notices of the Royal Astronomical Society* 495.3, pp. 3022–3040. DOI: 10.1093/mnras/staa1419.

Pakhomov, Y. V., T. A. Ryabchikova, and N. E. Piskunov (Dec. 2019). "Hyperfine Splitting in the VALD Database of Spectral-line Parameters". In: *Astronomy Reports* 63.12, pp. 1010–1021. DOI: 10.1134/S1063772919120047.

Poulain, M. et al. (Oct. 2021). "Structure and morphology of the MATLAS dwarf galaxies and their central nuclei". In: *Monthly Notices of the Royal Astronomical Society* 506.4, pp. 5494–5511. DOI: 10.1093/mnras/stab2092.

Reichert, M. et al. (Sept. 2020). "Neutron-capture elements in dwarf galaxies. III. A homogenized analysis of 13 dwarf spheroidal and ultra-faint galaxies". In: *Astronomy and Astrophysics* 641, A127, A127. DOI: 10.1051/0004-6361/201936930.

Revaz, Y. and P. Jablonka (Aug. 2018). "Pushing back the limits: detailed properties of dwarf galaxies in a ΛCDM universe". In: *Astronomy and Astrophysics* 616, A96, A96. DOI: 10.1051/0004-6361/201832669.

Rodriguez-Gomez, V. et al. (May 2016). "The stellar mass assembly of galaxies in the Illustris simulation: growth by mergers and the spatial distribution of accreted stars". In: *Monthly Notices of the Royal Astronomical Society* 458.3, pp. 2371–2390. DOI: 10.1093/mnras/stw456.

Rusakov, V. et al. (Mar. 2021). "The bursty star formation history of the Fornax dwarf spheroidal galaxy revealed with the HST". In: *Monthly Notices of the Royal Astronomical Society* 502.1, pp. 642–661. DOI: 10.1093/mnras/stab006.

Ryabchikova, T. et al. (May 2015). "A major upgrade of the VALD database". In: *Physica Scripta* 90.5, 054005, p. 054005. DOI: 10.1088/0031-8949/90/5/054005.

Salvatier, J., T. V. Wiecki, and C. Fonnesbeck (Oct. 2016). *PyMC3: Python probabilistic programming framework*. Astrophysics Source Code Library, record ascl:1610.016.

Sarajedini, A. and A. C. Layden (Mar. 1995). "A Photometric Study of the Globular Cluster M54 and the Sagittarius Dwarf Galaxy: Evidence for Three Distinct Populations". In: *The Astronomical Journal* 109, p. 1086. DOI: 10.1086/117343.

Sawala, T., C. Scannapieco, and S. White (Feb. 2012). "Local Group dwarf galaxies: nature and nurture". In: *Monthly Notices of the Royal Astronomical Society* 420.2, pp. 1714–1730. DOI: 10.1111/j.1365-2966.2011.20181.x.

Sawala, T. et al. (Apr. 2016). "The APOSTLE simulations: solutions to the Local Group's cosmic puzzles". In: *Monthly Notices of the Royal Astronomical Society* 457.2, pp. 1931–1943. DOI: 10.1093/mnras/stw145.

Schlegel, D. J., D. P. Finkbeiner, and M. Davis (June 1998). "Maps of Dust Infrared Emission for Use in Estimation of Reddening and Cosmic Microwave Background Radiation Foregrounds". In: *The Astrophysical Journal* 500.2, pp. 525–553. DOI: 10.1086/305772.

Schroyen, J. et al. (Sept. 2013). "Stellar orbits and the survival of metallicity gradients in simulated dwarf galaxies". In: *Monthly Notices of the Royal Astronomical Society* 434.1, pp. 888–905. DOI: 10.1093/mnras/stt1084.

Sestito, F. et al. (Apr. 2019). "Tracing the formation of the Milky Way through ultra metal-poor stars". In: *Monthly Notices of the Royal Astronomical Society* 484, pp. 2166–2180. DOI: 10.1093/mnras/stz043.

Simon, J. D. (Aug. 2019). "The Faintest Dwarf Galaxies". In: *Annual Review of Astronomy & Astrophysics* 57, pp. 375–415. DOI: 10.1146/annurev-astro-091918-104453.

Simon, J. D. et al. (Feb. 2021). "Eridanus II: A Fossil from Reionization with an Off-center Star Cluster". In: *The Astrophysical Journal* 908.1, 18, p. 18. DOI: 10.3847/1538-4357/abd31b.

Sneden, C. et al. (Feb. 2012). *MOOG: LTE line analysis and spectrum synthesis*. Astrophysics Source Code Library, record ascl:1202.009.

Sneden, C. A. (Jan. 1973). "Carbon and Nitrogen Abundances in Metal-Poor Stars." PhD thesis. University of Texas, Austin.

Starkenburg, E. et al. (Apr. 2010). "The NIR Ca ii triplet at low metallicity. Searching for extremely low-metallicity stars in classical dwarf galaxies". In: *Astronomy and Astrophysics* 513, A34, A34. DOI: 10.1051/0004-6361/200913759.

Starkenburg, T. K. and A. Helmi (Mar. 2015). "Dark influences: imprints of dark satellites on dwarf galaxies". In: *Astronomy and Astrophysics* 575, A59, A59. DOI: 10.1051/0004-6361/201425082.

Starkenburg, T. K., A. Helmi, and L. V. Sales (Mar. 2016a). "Dark influences II. Gas and star formation in minor mergers of dwarf galaxies with dark satellites". In: *Astronomy and Astrophysics* 587, A24, A24. DOI: 10.1051/0004-6361/201527247.

— (Oct. 2016b). "Dark influences. III. Structural characterization of minor mergers of dwarf galaxies with dark satellites". In: *Astronomy and Astrophysics* 595, A56, A56. DOI: 10.1051/0004-6361/201528066.

Stinson, G. et al. (Dec. 2006). "Star formation and feedback in smoothed particle hydrodynamic simulations - I. Isolated galaxies". In: *Monthly Notices of the Royal Astronomical Society* 373.3, pp. 1074–1090. DOI: 10.1111/j.1365-2966.2006.11097.x.

Taibi, S. et al. (Oct. 2018). "Stellar chemo-kinematics of the Cetus dwarf spheroidal galaxy". In: *Astronomy and Astrophysics* 618, A122, A122. DOI: 10.1051/0004-6361/201833414.

Tammann, G. A. (Jan. 1994). "Dwarf Galaxies in the Past". In: *European Southern Observatory Conference and Workshop Proceedings*. Vol. 49. European Southern Observatory Conference and Workshop Proceedings, p. 3.

Theler, R. et al. (Oct. 2020). "The chemical evolution of the dwarf spheroidal galaxy Sextans". In: *Astronomy and Astrophysics* 642, A176, A176. DOI: 10.1051/0004-6361/201937146.

Timmes, F. X., E. F. Brown, and J. W. Truran (June 2003). "On Variations in the Peak Luminosity of Type Ia Supernovae". In: *The Astrophysical Journal* 590.2, pp. L83–L86. DOI: 10.1086/376721.

Tolstoy, E., V. Hill, and M. Tosi (Sept. 2009). "Star-Formation Histories, Abundances, and Kinematics of Dwarf Galaxies in the Local Group". In: *Annual Review of Astronomy & Astrophysics* 47.1, pp. 371–425. DOI: 10.1146/annurev-astro-082708-101650.

Tolstoy, E. et al. (Dec. 2004). "Two Distinct Ancient Components in the Sculptor Dwarf Spheroidal Galaxy: First Results from the Dwarf Abundances and Radial Velocities Team". In: *The Astrophysical Journal* 617.2, pp. L119–L122. DOI: 10.1086/427388.

Travaglio, C., W. Hillebrandt, and M. Reinecke (Dec. 2005). "Metallicity effect in multi-dimensional SNIa nucleosynthesis". In: *Astronomy and Astrophysics* 443.3, pp. 1007–1011. DOI: 10.1051/0004-6361:20052883.

Walker, M. G., M. Mateo, and E. W. Olszewski (Dec. 2008). "Systemic Proper Motions of Milky Way Satellites from Stellar Redshifts: The Carina, Fornax, Sculptor, and Sextans Dwarf Spheroidals". In: *The Astrophysical Journal Letters* 688.2, p. L75. DOI: 10.1086/595586.

— (Feb. 2009). "Stellar Velocities in the Carina, Fornax, Sculptor, and Sextans dSph Galaxies: Data From the Magellan/MMFS Survey". In: *The Astronomical Journal* 137.2, pp. 3100–3108. DOI: 10.1088/0004-6256/137/2/3100.

Walker, M. G. et al. (May 2006). "On Kinematic Substructure in the Sextans Dwarf Spheroidal Galaxy". In: *The Astrophysical Journal* 642.1, pp. L41–L44. DOI: 10.1086/504522.

Walker, M. G. et al. (Aug. 2007). "The Michigan/MIKE Fiber System Survey of Stellar Radial Velocities in Dwarf Spheroidal Galaxies: Acquisition and Reduction of Data". In: *The Astrophysical Journal Supplement Series* 171.2, pp. 389–418. DOI: 10.1086/517886.

White, S. D. M. and M. J. Rees (May 1978). "Core condensation in heavy halos: a two-stage theory for galaxy formation and clustering." In: *Monthly Notices of the Royal Astronomical Society* 183, pp. 341–358. DOI: 10.1093/mnras/183.3.341.

Willman, B. and J. Strader (Sept. 2012). ""Galaxy," Defined". In: *The Astronomical Journal* 144.3, 76, p. 76. DOI: 10.1088/0004-6256/144/3/76.

York, D. G. et al. (Sept. 2000). "The Sloan Digital Sky Survey: Technical Summary". In: *The Astronomical Journal* 120.3, pp. 1579–1587. DOI: 10.1086/301513.

Zoutendijk, S. L. et al. (Mar. 2020). "The MUSE-Faint survey. I. Spectroscopic evidence for a star cluster in Eridanus 2 and constraints on MACHOs as a constituent of dark matter". In: *Astronomy and Astrophysics* 635, A107, A107. DOI: 10.1051/0004-6361/201936155.